metals

MDPI

Article

On the Influence of Control Type and Strain Rate on the Lifetime of 50CrMo4

Max Benedikt Geilen [1,*], Josef Arthur Schönherr [1], Marcus Klein [1], Dominik Sebastian Leininger [1], Alexander Giertler [2], Ulrich Krupp [3] and Matthias Oechsner [1]

[1] Centre for Engineering Materials (MPA-IfW), Technical University of Darmstadt, Grafenstraße 2, 64283 Darmstadt, Germany; schoenherr@mpa-ifw.tu-darmstadt.de (J.A.S.); m.klein@mpa-ifw.tu-darmstadt.de (M.K.); dominik.leininger@t-online.de (D.S.L.); oechsner@mpa-ifw.tu-darmstadt.de (M.O.)

[2] Institute of Materials Design and Structural Integrity, Osnabrück University of Applied Sciences, Albrechtstraße 30, 49009 Osnabrück, Germany; a.giertler@hs-osnabrueck.de

[3] IEHK Steel Institute, RWTH Aachen University, Intzestraße 1, 52072 Aachen, Germany; krupp@iehk.rwth-aachen.de

* Correspondence: geilen@mpa-ifw.tu-darmstadt.de; Tel.: +49-6151-16-25867

Received: 5 October 2020; Accepted: 27 October 2020; Published: 30 October 2020

Abstract: In this study, we investigate the influence of control type and strain rate on the lifetime of specimens manufactured from 50CrMo4. This influence is described by a strain rate dependent method that uses cyclic stress strain curves to correct displacement-controlled cyclic test results. The objective of this correction is to eliminate the stress related differences between displacement-controlled cyclic test results and force-controlled cyclic test results. The method is applied to the results of ultrasonic fatigue tests of six different combinations of heat treatment, specimen geometry (notch factor) and atmosphere. In a statistical analysis, the corrected results show an improved agreement with test results obtained on conventional fatigue testing equipment with similar specimens: the standard deviation in combined data sets is significantly reduced (p = 4.1%). We discuss the literature on intrinsic and extrinsic strain rate effects in carbon steels.

Keywords: ultrasonic cyclic testing; frequency effect; control type effect; strain rate effect; 50CrMo4; SAE 4150; high cycle fatigue; very high cycle fatigue; statistical analyses

1. Introduction

Since the early days of fatigue research, stress based approaches have been used for the fatigue design of components. This approach prevails in the high cycle fatigue (HCF) region to this day. Models of this kind are best calibrated using stress-controlled cyclic tests. In the 1950s and 1960s, strain-based approaches, which differentiate between elastic and plastic strain, were developed to improve predictive power in the low cycle fatigue (LCF) region [1]. Strain-based models are best calibrated using strain-controlled fatigue tests. In the 1980s and 1990s, component failures in the gigacycle range kick-started very high cycle fatigue (VHCF) research [2–12]. In VHCF fatigue initiation, no macroscopically plastic material behavior is observed, therefore stress based models are employed. Ideally, these models should be calibrated using stress-controlled cyclic tests.

Materials testing in the VHCF region is conducted on two kinds of fundamentally different testing setups. The first kind are conventional testing machines—e.g., resonance or servo-hydraulic testing machines—which are also used in the HCF region. These machines are able to operate under stress control but rarely exceed testing frequencies of 200 Hz. While some state of the art testing machines like

Rumul Gigaforte 50 reach up to 1000 Hz, typical testing frequencies range from 20 to 100 Hz. The second kind is ultrasonic fatigue testing machines. Ultrasonic fatigue testing machines run at 20 kHz but must be run in pulse pause mode because of a material-dependent specimen's self-heating. They usually reach effective testing frequencies of 2 kHz. Depending on geometry, tolerated temperature increase, material under investigation, load level and cooling equipment, the effective testing frequency varies. Ultrasonic testing machines operate under displacement control [13]. In cyclically softening steel specimens under displacement control, notch stress amplitudes may decrease over the course of the cyclic test.

In research on low strength (ultimate tensile strength 919 MPa) cyclically softening 50CrMo4 [10], differences between the results of displacement-controlled cyclic tests conducted at about 20 kHz and the results of force-controlled cyclic tests conducted between 20 Hz and 700 Hz were observed. Such differences have largely been attributed to a frequency or strain rate effect [6,14–19]. In research on high strength (ultimate tensile strength 1726 MPa) 50CrMo4, the observed differences between such tests were remarkably smaller, which has been attributed to a lower strain rate influence for high strength steels [6]. The understanding of these test results without further processing is limited by the coupling between strain rate and control type.

In components testing, displacement-controlled cyclic tests are conducted to simultaneously test dozens of specimens with a single testing machine [20], which allows testing much larger numbers of specimens at a given budget. These results should be used to design force-loaded components only after correction for control type.

In this study, an algorithm [21] implementing a method for the strain rate dependent correction for control type [10] is utilized to create control type corrected cyclic test results from displacement-controlled cyclic test results for different batches of 50CrMo4. We show that for each batch, these corrected results show an equal or improved agreement with results of force-controlled cyclic tests in the HCF range.

In Section 2, an overview on strain rate effects in fatigue is given. In Section 3, the data used in this investigation are described. In Section 4, the numerical methods of the investigation are described. In Section 5 and 6 , the results of the investigation are presented and analyzed. In Section 7, the investigation is summarized and in Section 8, an outlook is given.

2. Effects of Strain Rate on Deformation and Fatigue

A multitude of studies on fatigue life were conducted at different strain rates on steels [6,16,19,22–32] as well as other materials [22,33–43]. The results of these studies are mixed, some showing momentous differences in fatigue life, some showing ambiguous results, implying that there is no significant strain rate influence in these investigations. In this section, we describe different effects suspected to cause strain rate effects.

Frequency and strain rate effects may be divided into intrinsic effects and extrinsic effects [14]. Effects are called intrinsic if they are caused directly by strain rate dependent material behavior. An intrinsic effect at microscopic scale is a change in the formation process of slip bands or an activation of dynamic strain aging effects. These effects at microscopic scale cause effects at macroscopic scale, for example an increase in monotonic and cyclic yield strength. These effects are well studied for monotonic loading [44–52]. For cyclic loading, fewer studies are available [41,42,45,53]. Extrinsic effects are effects that sometimes or always accompany strain rate effects, but are at least in theory separable from intrinsic strain rate effects. Important extrinsic effects are temperature, hydrogen and chlorine concentration in the crack tip due to diffusion, control type, testing volume and oxidation-induced crack closure.

2.1. Intrinsic Effects

Since cyclic deformation is the sum of a succession of monotonic deformations, it is natural to assume that qualitatively, the same effects apply for monotonic and cyclic deformations. Therefore,

we first explain the much better studied monotonic effects on deformation behavior. While the strain rate dependency is fundamentally different for some materials [54], we will focus on the description of the state of research on carbon steels.

At microscopic scale, strain rate is closely linked to the activation energy of dislocations. For dislocations to form or move, a certain energy must be supplied locally [50]. In a given material at a given temperature and strain state, this is a stochastic process with an average rate of dislocations forming and moving per (unit) volume. At higher strain rates, the finite dislocation velocity is not sufficient to accommodate the fixed displacement rate, leading to a higher macroscopic yield stress. Higher strain rates influence the microscopic behavior very similarly to lower temperatures: at a given Peierls stress and a given stress state, fewer dislocations form or move. With increasing temperature, activation energies increase, helping dislocations to move, which explains the observation of lower strain rate sensitivities of flow stresses at 800 °C compared to 25 °C [50]. Between these temperature levels, a maximum in strain rate sensitivity of flow stress is expected due to strain aging. Strain aging is caused by Cottrell atmospheres—carbon atoms pinned in dislocations, necessitating high (localized) forces to unpin and thereby raising the (localized) force necessary to move the dislocation.

At high strain rates, adiabatic conditions promote locally high temperatures. These locally high temperatures promote the strongly localized formation of shear bands: in the formation of dislocations, only a portion of the expended energy is introduced into the crystal structure, another portion is converted into heat [55], which leads to a locally higher temperature because at very high strain rates, heat conduction is slow compared to heat generation. The higher temperature again facilitates the generation of new dislocations, in which new heat is generated, leading to a cycle only broken by the removal of the source of increasing strain. This may be a fracture event in monotonic loading or the onset of unloading in cyclic loading. In the adiabatic regions, recrystallization may occur [56]. In cyclic loading, strongly localized temperature increase depends on load level and pulse length. While the global increase of temperature is well controlled by pulse pause methods, true localized temperatures remain unknown to researchers. Localized temperatures in adiabatic conditions may be computed based on a factor determining the share of energy converted into heat [50,57,58]. This factor has been determined to be close to 100% [57].

On the macroscopic scale, yield stress and ultimate tensile strength increase with increasing strain rate [44,50,59,60]. A widespread model describing this relationship is the Johnson Cook model [61].

From a fracture mechanics point of view, fatigue is a crack growing from a pre-existing defect. This defect may be e.g., an inclusion in the material, a scratch or in- and extrusions caused by persistent slip bands. Crack growth rate is determined by an intrinsic crack growth curve and crack closure effects [62]. Crack growth experiments on 32CrMo4 showed no overall influence of frequency (varied between 0.02 Hz and 20 Hz, measured in the Paris range) on the overall crack growth rate [63]. This has been interpreted as absence of an influence of strain rate on the intrinsic crack growth curve [64]. To draw a generally applicable conclusion, more evidence is necessary, firstly regarding higher strain rates and secondly regarding a wider range of carbon steels.

Plasticity-induced crack closure [62,65–70] depends on strain rate because plasticity depends on strain rate. Kindly note that although the change in plasticity-induced crack closure is an intrinsic effect with regard to intrinsic or extrinsic strain rate effects, the intrinsic crack growth curve is the one measured without any plasticity-induced (or other) crack closure. For small polished specimens, the influence of plasticity-induced crack closure is probably small since loads at the crack tip are below the crack growth threshold until shortly before failure.

No fundamental difference has been observed between the strain rate dependencies of deformations under cyclic compressive and cyclic tensile loads [45].

2.2. Extrinsic Effects

Specimens with larger critically loaded surface areas and volumes show decreased lifetimes compared to specimens with smaller critically loaded surfaces and volumes. This phenomenon

is well-studied [71–84] and understood well enough to be included in design standards [85–87]. Ultrasonic fatigue specimens, i.e., all specimens used for very high strain rate fatigue tests, are generally small-sized. This introduces a bias if the size effect is not accounted for. Jeddi and Palin-Luc [15] show that size effects explain the difference in results with different strain rates for several studies [23,24,27], which implies that there is no relevant strain rate effect in these studies. In their analysis, a model assuming that fatigue strength is inversely proportional to specimen diameter is utilized. This model is meant to consider the effect of the critically loaded surface and volume, a consideration of the crack growth phase is not explicitly intended. They [15] conclude that for high strength steels in general, there is no relevant strain rate effect on the fatigue behavior.

Another extrinsic effect is oxide-induced crack closure [62,65,67,69,88–91], which is caused by the following process: the outermost layer of the steel at the flanks of the crack is oxidized over time due to exposure to oxygen. Due to the oxidation, the volume of the outermost layer of the crack is increased. Due to the increased volume, the crack closes at higher loads. This leads to the crack being open for a lower portion of the load cycle, which leads to the generation of fewer dislocations and therefore a lower amount of crack growth per cycle [92]. Although the usual thickness of oxide layers is only a few nanometers, at the crack flanks, the oxide layer may grow to a significant size due to continuous breaking and reforming due to fretting contact between both crack flanks [69]. Since at lower frequencies, more time passes between two cycles, the oxidation effect is stronger and the crack grows slower (less per cycle, not per time) than at higher frequencies. This implies a longer lifetime for low frequencies compared to high frequencies in the absence of other effects. This effect does not occur at high load ratios since the oxide layer is not sufficient to close the crack at high stresses.

Note that the oxide-induced crack closure effect does not dominate the influence of the atmosphere: the average lifetime of specimens tested in argon is longer than that of specimens tested in lab air all else being equal, Section 5. A momentous difference has also been registered between dry air and humid air [93]. This effect has been reported to be pronounced in quenched 42CrMo4 steels [93]. The effect has been shown to decrease with tempering, ceasing to exist in 42CrMo4 tempered at 550 °C for 1 h [93]. For a high hardness batch of 42CrMo4, no obvious difference has been observed in the fatigue life of specimens in high humidity air and specimens in high humidity argon, however it remains unclear if residual adsorbed oxygen in the specimens in argon may be responsible for the behavior [93]. For a 1076 MPa ultimate tensile strength batch of 41NiCrMo7-3-2 steel, slightly higher lifetimes were observed for specimens tested in dry air compared to specimens tested in humid air [94]. For 0.5% carbon steel, momentously longer lifetimes and a higher fatigue limit were observed in vacuum [95]. For 41NiCrMo7-3-2 [96] and 100Cr6 at a high load level [97], slightly longer lifetimes were observed in vacuum compared to lab air [96]. Specimens manufactured from 100Cr6 with artificial surface defects showed higher survival probabilities in lab air than in vacuum when tested at the same load level up to 2×10^9 cycles. Crack growth was observed to accelerate with increasing humidity in argon [98] and air [99,100]. In vacuum, reduced crack growth rates were observed in comparison to lab air [101,102].

The reduced fatigue performance in humid air and argon is largely blamed on the prevention of slip reversal—a mechanism that increases lifetime—in oxidizing environments in general [103–105]. Slip reversal occurs when dislocations are moved along a slip band onto the surface of the specimen during loading and are subsequentially moved back into their old position during unloading. This way, no damage accumulates and therefore, no contribution to failure is made. Adsorption of oxygen may prevent the reverse movement, which makes the slip irreversible [106]. Irreversible slip bands lead to intrusions and extrusions, which may nucleate a crack.

The oxide layers on the surface may have a higher Young's modulus than the base steel. If that's the case, for dislocations to pass the interface, an additional force must be expended. This leads to pileups of dislocations just under the oxide layer, which promote crack initiation [105]. Aluminum shows a momentous influence of environment, however, it has been shown that the surface oxide has a lower Young's modulus than the base metal [107,108].

The environment of internal cracks may be viewed as a vacuum. This view is supported by similar fracture surfaces [96,97,109]. The sometimes distinct segregation of cracks initiating from the surface and cracks initiation from sub-surface with respect to the number of cycles to failure has been attributed to the difference in crack initiation times in vacuum in comparison to lab air [110]. For a batch of JIS-SNCM439, segregation was observed to be present if tests were conducted in lab air but not if tests were conducted in vacuum [96].

In steels, hydrogen is present to some degree, although this degree is very low in high quality steel. Some research [111,112] suggests that VHCF failure from inclusions is connected to hydrogen, even if hydrogen concentrations are not measurable. This may be caused by an inhomogeneous distribution of hydrogen in the specimen: hydrogen does not really follow Fick's law in its diffusion behavior but concentrates at points of high tensile stress. At low strain rates hydrogen has a lot of time to diffuse to the crack tip, at higher strain rates it has less time because the crack tip moves faster. The increased hydrogen concentration implies shorter lifetimes for lower strain rates. In theory, all the hydrogen in the whole specimen diffuses to an infinitesimal small volume around the crack tip because of the stress singularity. The reality is of course less extreme. More on the interaction between hydrogen diffusion and plasticity may be found in [113,114]. If hydrogen is introduced into or removed from the specimen in any way during cyclic loading, this is a time dependent and therefore indirectly strain rate dependent process. In specimens charged with hydrogen, crack growth rates increase momentously with decreasing frequencies [64]. In uncharged austenitic specimens, crack growth rates increase with decreasing frequencies, which has been attributed to non-diffusible hydrogen [64]. In uncharged 34CrMo4 specimens, an increase of crack growth rate with decreasing frequency has not been observed, which may be due to the much higher diffusivity of hydrogen [63,64]. These studies were conducted at low strain rates. Due to the higher diffusivity, hydrogen diffusion may become more influential in carbon steels at higher strain rates, however to our knowledge, there is no experimental evidence available on this issue.

3. Experimental Foundation

In this work, the cyclic properties of the quenched and tempered steel 50CrMo4 are investigated. The material was provided in five batches, having different tempering states with ultimate tensile strengths σ_u of 919 MPa, 1096 MPa, 1170 MPa, 1475 MPa and 1726 MPa. Its chemical compositions are given in Table 1 and tensile test results are given in Table 2.

Most data were obtained in two research projects on the influence of variable amplitude loading in the VHCF range, conducted at the Centre for Engineering Materials (MPA-IfW) and Fraunhofer LBF Darmstadt [5,6,10]. These are all data belonging to the material batches with tensile strengths of 919 MPa, 1170 MPa, 1475 MPa and 1726 MPa. The testing machines used therein for cyclic testing are a 20 kHz ultrasonic testing system (USP), type BOKU Vienna UFTE, a 700 Hz electromechanic test system (EMF) and a 400 Hz servo-hydraulic testing machine (VHF), type Instron Schenck VHF 50D. The results were obtained at testing frequencies of about 19 kHz for the USP, 700 Hz for the EMF and 20–200 Hz for the VHF.

Table 1. Chemical composition (in weight percent).

Material Batch	C	Cr	Mo	Mn	P	S
919 MPa [5]	0.53	1.06	0.19	0.69	<0.01	<0.01
1096 MPa [8]	0.48	1.00	0.18	0.71	0.013	0.010
1170 MPa [10]	0.49	1.01	0.19	0.69	<0.01	0.011
1475 MPa [10]	0.48	1.06	0.19	0.68	0.01	0.012
1726 MPa [6]	0.51	1.09	0.19	0.73	0.016	<0.01

Table 2. Tensile test results.

Material Batch	Young's Modulus E in GPa	0.2% Offset Yield Strength $\sigma_{0.2}$ in MPa	Ultimate Tensile Strength σ_u in MPa
919 MPa [5]	206	842	919
1096 MPa [8]	202	1000	1096
1170 MPa [10]	208	1025	1170
1475 MPa [10]	204	1345	1475
1726 MPa [6]	215	1544	1726

For further validation, test data were provided by Osnabrück University of Applied Sciences [8,115], obtained at 20 kHz with an ultrasonic testing system (USPO) type BOKU Vienna and at about 95 Hz, obtained with a electromechanic resonance testing machine, type Rumul Testronic (RTTO). The investigated material was quenched and tempered to an ultimate tensile strength of 1096 MPa.

The ultrasonic testing equipment was operated in pulse pause mode. All tests were conducted at ambient temperature. The load ratio was fixed to $R = -1$. At load ratios of -1, no cyclic creep is observed in quenched and tempered carbon steel [116]. Therefore, cyclic creep is ignored in this publication.

The fatigue specimen geometries are depicted in Figures 1–4. The metallographic characterization of these specimens showed no irregularities relevant for this investigation; for more details see [5,6,10,115].

To assess the material behavior at high strain rates, fast tensile tests were conducted on a high speed tensile testing machine. On the left hand side of Figure 5, the ultimate tensile strength results for the 919 MPa batch as well as a bi-linear approximation thereof are shown. On the right hand side, these data are combined with data from the 1170 MPa batch and from the 1475 MPa batch. For comparison, the stress is normalized to the particular quasi-static ultimate tensile strength, see Table 2. All three materials show a good agreement in their relative 0.2% offset yield strength $\sigma_{0.2}$. In the tests on the 1170 MPa batch at strain rates of about 15/s, two outliers were observed. In a comparative metallographic examination of an outlier specimen and a non-outlying specimen, the outlier showed a significantly different microstructure. In this investigation, the outliers are considered in the process of fitting the bi-linear curve to uphold consistency, since not all specimens were investigated with regard to their microstructure. The fatigue behaviors of the batches 1170 MPa and 1475 MPa are not assessed in this study because the inhomogenities in the microstructure state were also observed in some cyclic test specimens, and therefore, the comparability of the fatigue behavior is limited.

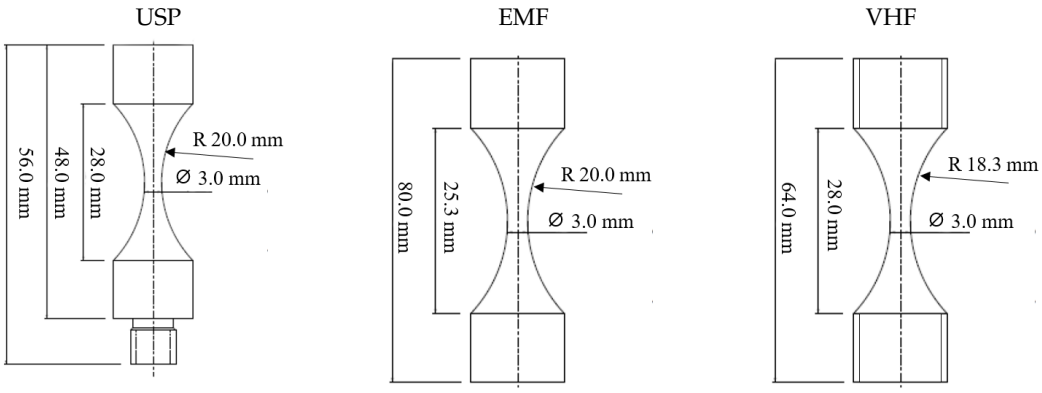

Figure 1. Geometry of specimens with ultimate tensile strength 919 MPa and K = 1 [9,10,21].

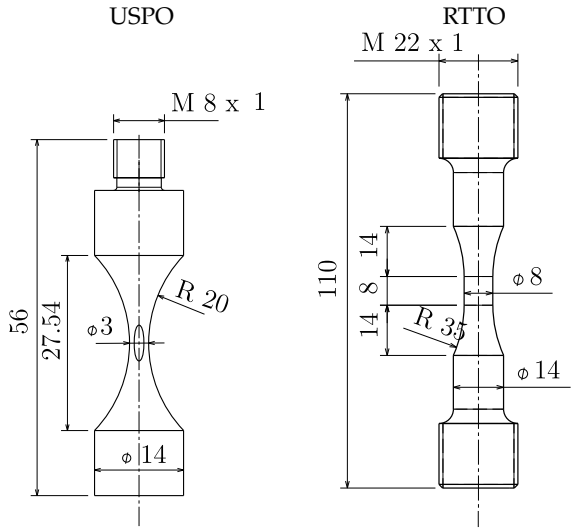

Figure 2. Geometry of specimens with ultimate tensile strength 1096 MPa and K = 1.2 [8,115].

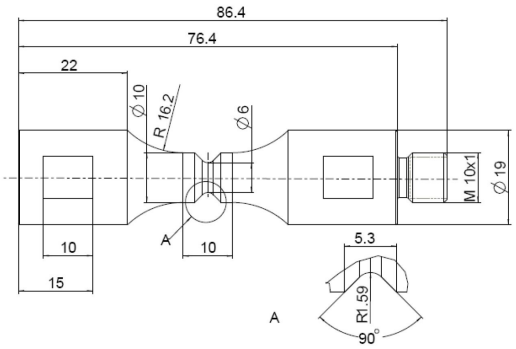

Figure 3. Geometry of ultrasonic testing system (USP) specimens with ultimate tensile strength 919 MPa and K = 1.75 [6], VHF specimens were finalized subsequently [9].

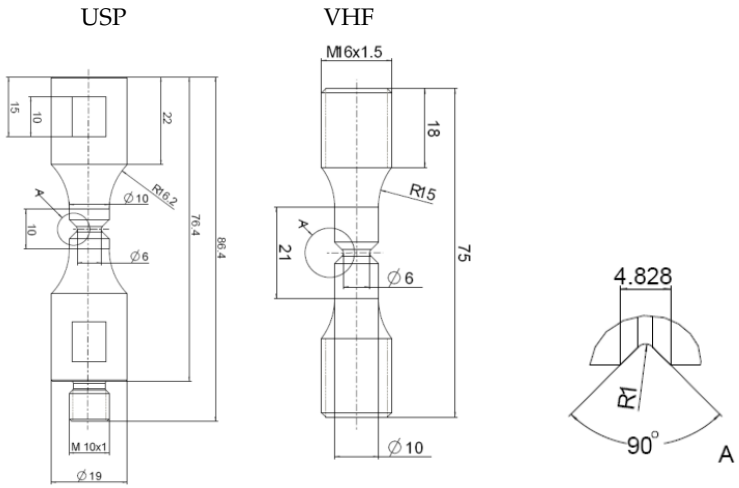

Figure 4. Geometry of specimens with ultimate tensile strength 919 as well as 1726 MPa and K = 2.06 [6].

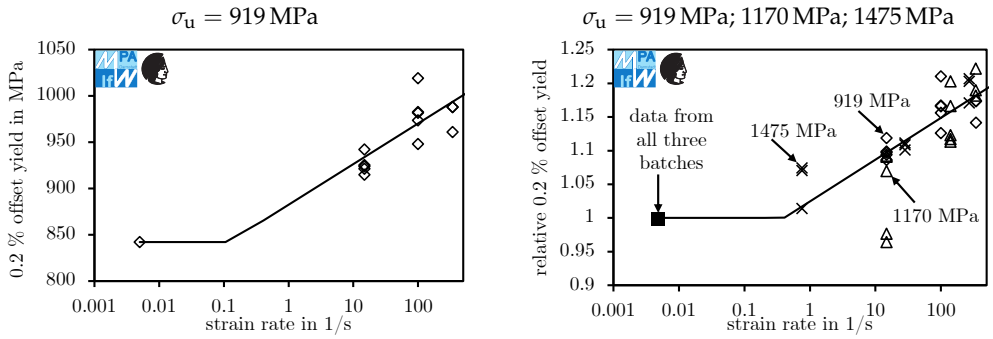

Figure 5. This figure shows 0.2% offset yield depending on the strain rate, for the 919 MPa ultimate tensile strength (**left**) and for the batches 919 MPa, 1170 MPa and 1475 MPa (**right**).

In Figure 6, the stabilized cyclic stress strain test results are shown. The left diagrams show test results for the 919 MPa and 1726 MPa batch. These results were obtained in five constant amplitude tests each. On the right-hand side, the results for the 1096 MPa batch are given in the first row. These were obtained in an Incremental Step Test. As shown in the bottom right diagram, the test results fit together well, since the stress amplitude over strain amplitude values increase with the quasi-static ultimate tensile strength of the material, regardless of the test setting.

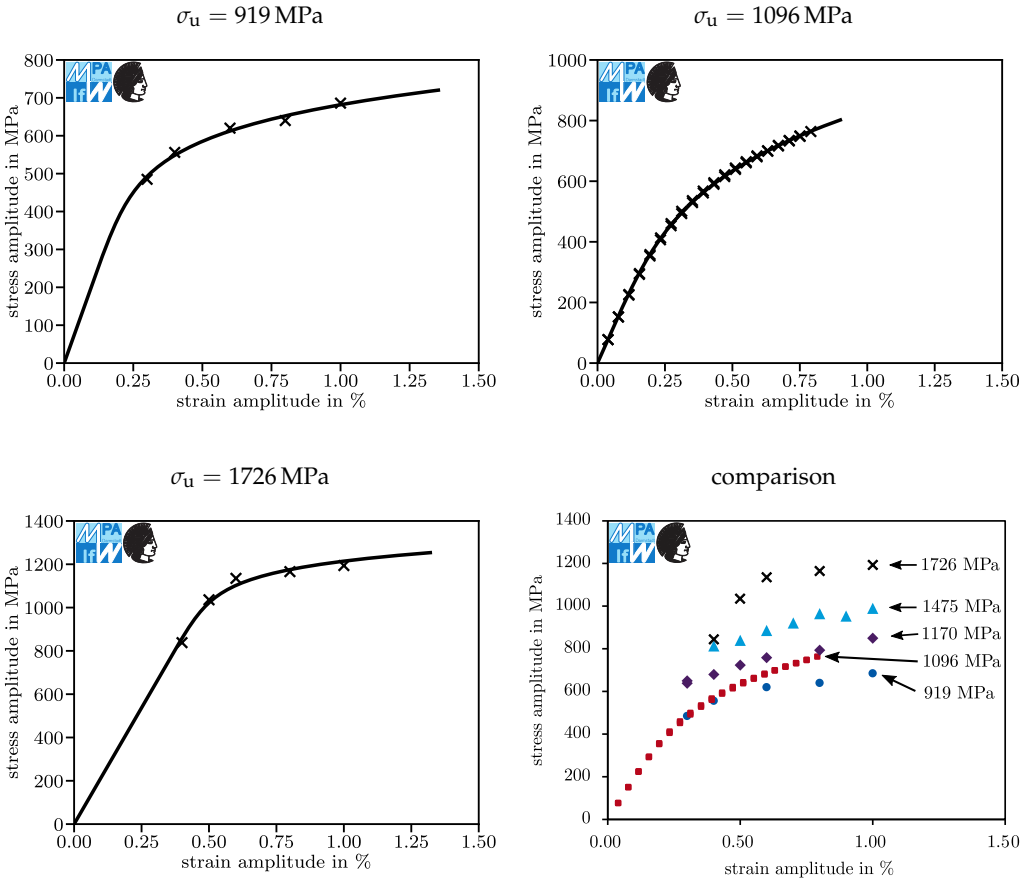

Figure 6. Cyclic stress strain curves. (**First row**): 919 MPa and 1096 MPa ultimate tensile strength. (**Second row**): 1726 MPa ultimate tensile strength (left) and comparison of batches with 919 MPa, 1096 MPa, 1170 MPa, 1475 MPa and 1726 MPa ultimate tensile strength.

The cyclic stress strain curve was generated in a least squares fit in stress direction using the Ramberg–Osgood formulation [117],

$$\varepsilon_a = \epsilon_{a,el} + \epsilon_{a,pl} = \frac{\sigma_a}{E} + \left(\frac{\sigma_a}{K'}\right)^{1/n'}, \quad (1)$$

where ε_a is the strain amplitude, σ_a is the stress amplitude, K' is the cyclic hardening coefficient and n' is the cyclic hardening exponent. The parameters obtained for the cyclic stress strain curves provided in the previous figures are summarized in Table 3.

Table 3. Cyclic material constants.

Material Batch	Young's Modulus E in GPa	Hardening Coefficient K' in MPa	Hardening Exponent n'
919 MPa	206	1341	0.135
1096 MPa	202	2816	0.237
1170 MPa	204	1162	0.068
1475 MPa	204	1436	0.073
1726 MPa	215	1687	0.060

4. Method

4.1. Correction for Control Type

The stress levels of displacement-controlled tests are corrected using the Neuber rule [118,119]. Therein, cyclic stress strain curves are used. These curves were obtained either from constant amplitude tests or from Incremental Step Tests by fitting a Ramberg–Osgood curve [117], Figure 6. These Ramberg–Osgood curves are corrected for the specific strain rate, assuming that the cyclic offset yield strength increases proportionally to the monotonous offset yield strength with increasing strain rate. The monotonous offset yield strength was modeled by a bi-linear function in log-lin space, Figure 5. A constant strain rate is assumed, while the strain rate in fact is sinusoidal; the computed strain rate is equal to the real average strain rate.

The strain amplitude ϵ_a according to Ramberg–Osgood is computed as the sum of the elastic strain amplitude $\epsilon_{a,el}$ and the plastic strain amplitude $\epsilon_{a,pl}$, which may be computed from the stress amplitude σ_a, the 0.2% offset yield strength $\sigma_{0.2}$, the yield offset α, Young's modulus E and the cyclic hardening exponent n' :

$$\epsilon_a = \epsilon_{a,el} + \epsilon_{a,pl} = \frac{\sigma_a}{E} + \alpha \frac{\sigma_a}{E} \left(\frac{\sigma_a}{\sigma_{0.2}}\right)^{1/n'-1} \quad (2)$$

This formulation differs from the formulation in Equation (1) only in the variables used, the relationship between the variables is:

$$\alpha = \left(\frac{E}{K'}\right)^{1/n'} \left(\frac{\sigma_{0.2}}{E}\right)^{1/n'-1} \quad (3)$$

Here, the less customary version of the formula is used because the offset yield strength $\sigma_{0.2}$ is explicit, which is advantageous for the algorithm. The yield offset α is computed as:

$$\alpha = \frac{0.002\ E}{\sigma_{0.2}} \quad (4)$$

The cyclic offset yield strength $\sigma_{0.2}$ is strain rate dependent and therefore computed based on the ratio of the strain rate $\dot{\epsilon}$ and the reference strain rate $\dot{\epsilon}_{\text{ref}}$. To model the behavior, the bi-linear function x is used:

$$\sigma_{0.2}(\dot{\epsilon}) = \sigma_{0.2}(\dot{\epsilon}_{\text{ref}}) \cdot x\left(\frac{\dot{\epsilon}}{\dot{\epsilon}_{\text{ref}}}\right) \tag{5}$$

The strain rate $\dot{\epsilon}$ is computed using the strain amplitude ϵ_{a} and the frequency f, assuming that the strain rate was constant during a single fatigue test:

$$\dot{\epsilon} = 4 \cdot \epsilon_{\text{a}} \cdot f \tag{6}$$

Neuber's rule is applied by finding the point in the Ramberg–Osgood formulation of the cyclic material behavior (Equation (2)) for which the strain energy density is equal to the strain energy density in the elastic computation, which is derived from the elastically computed stress amplitude and the elastically computed strain amplitude :

$$\min_{\sigma_{\text{a}}}(\sigma_{\text{a}} \cdot \epsilon_{\text{a}}(\sigma_{\text{a}}) - \sigma_{\text{a,elastic}} \cdot \epsilon_{\text{a,elastic}})^2 \tag{7}$$

Since the Ramberg–Osgood formulation is not static but depends on the strain rate, the optimization problem is solved iteratively and in each iteration, the strain rate from the last iteration is used. The solving of the minimization problem is repeated until the change in $\dot{\epsilon}$ over an iteration comes below a threshold. For this investigation, the threshold 10^{-15} was used. The computation procedure is displayed in Figure 7. Due to the iterative character of the algorithm, an index i is added to some variables.

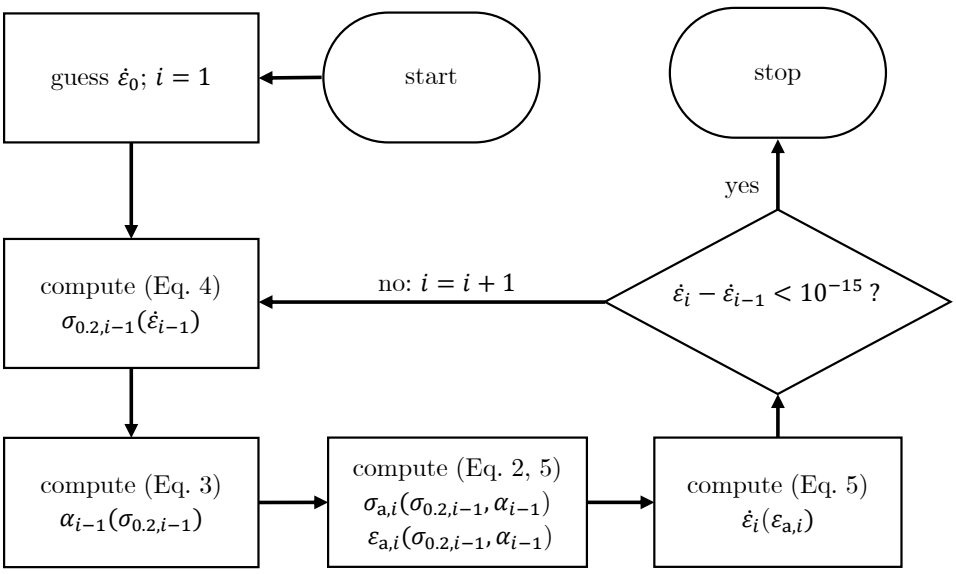

Figure 7. Algorithm used in this study to compute corrected load levels.

An earlier version of the algorithm used herein is described in [21]. The difference between both versions of the algorithm is that the algorithm used herein models the offset yield strength as a bi-linear function, while the algorithm described there utilizes a linear function. The change made for this study leads to slightly smaller correction offsets at high strain rates and slightly higher offsets at low strain rates (as long as these low strain rates are above the lowest strain rate tested). The change is motivated by the fact that for medium to low strain rates, the offset yield strength is not a function of the strain rate.

4.2. Statistical Analysis

The goal of the correction is to create data from displacement-controlled cyclic tests that agree well with data from force-controlled cyclic tests. To evaluate whether the agreement is improved by the correction, a statistical analysis is conducted. Two types of data sets are created, merging results of displacement-controlled cyclic tests before (type 1) and after (type 2) correction with results of force-controlled cyclic tests.

For each data set, a lifetime model assuming a linear course of the fatigue curve in log-log space and a constant log-normal distribution of fracture cycles at given load levels is fitted to all events occurring at up to 3×10^6 cycles, using the maximum likelihood method. For these models, the standard deviation is estimated in the fitting process.

The log-normal distribution is generally accepted as a good approximation of the fatigue behavior of steels in the HCF range [120–123]. Overall, the assumption of log-normality is reasonable, although some of the data sets under investigation deviate significantly from log-normal distributions: in data sets with two populations that differ from each other in their average lifetimes at a given load level (e.g. due to different control types), the assumption of a log-normal distribution is obviously not true. More data on the question whether the data sets under investigations are well described by models using constant log-normal distributions may be found in Appendix A.

The estimated standard deviation provides an intuitive measure of the agreement between two underlying data sets: if the points of both data sets are far away from each other, the estimated standard deviation is high and the intuitively estimated agreement is low. If the points of each data set are close to the point of the other data set, the estimated standard deviation is low and the intuitively estimated agreement is high.

To further reduce subjectivity, the agreement is also evaluated using the mathematically motivated measure of the log-likelihood function. A higher log-likelihood value implies a better agreement of all data in the data set and therefore also implies a better agreement between both merged data sets. Therefore, the log-likelihood value is used as a more objective comparative measure of agreement.

5. Results

All tests performed with electromagnetic and servo-hydraulic testing machines were conducted force-controlled, whereas the ultrasonic testing system operates displacement-controlled. In Figure 8, the fatigue behavior, namely the stress amplitudes plotted against the number of cycles for specimens quenched and tempered to ultimate tensile strength levels of 919 MPa are given. The tests were conducted with unnotched round specimens (stress concentration factor $K_t = 1$) in laboratory air. On the left hand side, a purely elastic material law was used for evaluation. The data presented there have not undergone any correction. On the right hand side, the displacement-controlled test results were corrected using the elastic-plastic material law given in Section 3 and the method described in Section 4.1. The continuous lines depict the fatigue curves for 50% survival probability, the dashed ones for 10% and 90%, respectively. The curves were generated using the maximum likelihood method, fitting the slope exponent k_1, the standard deviation SD and a reference point of the fatigue curve. The fatigue curve describes a field of failure probability densities f with the reference logarithmic number of cycles $N_{\mathrm{ref,log}}$, the reference logarithmic normalized stress amplitude $\sigma_{\mathrm{ref,log}}$ and the standard deviation SD that depends on the logarithm of the number of cycles N_{log} and the logarithm of the normalized stress amplitude $\sigma_{\mathrm{amplitude,log}}$:

$$f(N_{\mathrm{log}}, \sigma_{\mathrm{amplitude,log}}) = \frac{1}{\sqrt{2\pi SD^2}} \exp\left(- \frac{\left(N_{\mathrm{log}} - N_{\mathrm{ref,log}} - \left(\sigma_{\mathrm{amplitude,log}} - \sigma_{\mathrm{ref,log}} \right) \cdot k_1 \right)^2}{2\, SD^2} \right) \quad (8)$$

For the generation of these curves, only events occurring at up to 3×10^6 cycles were taken into account.

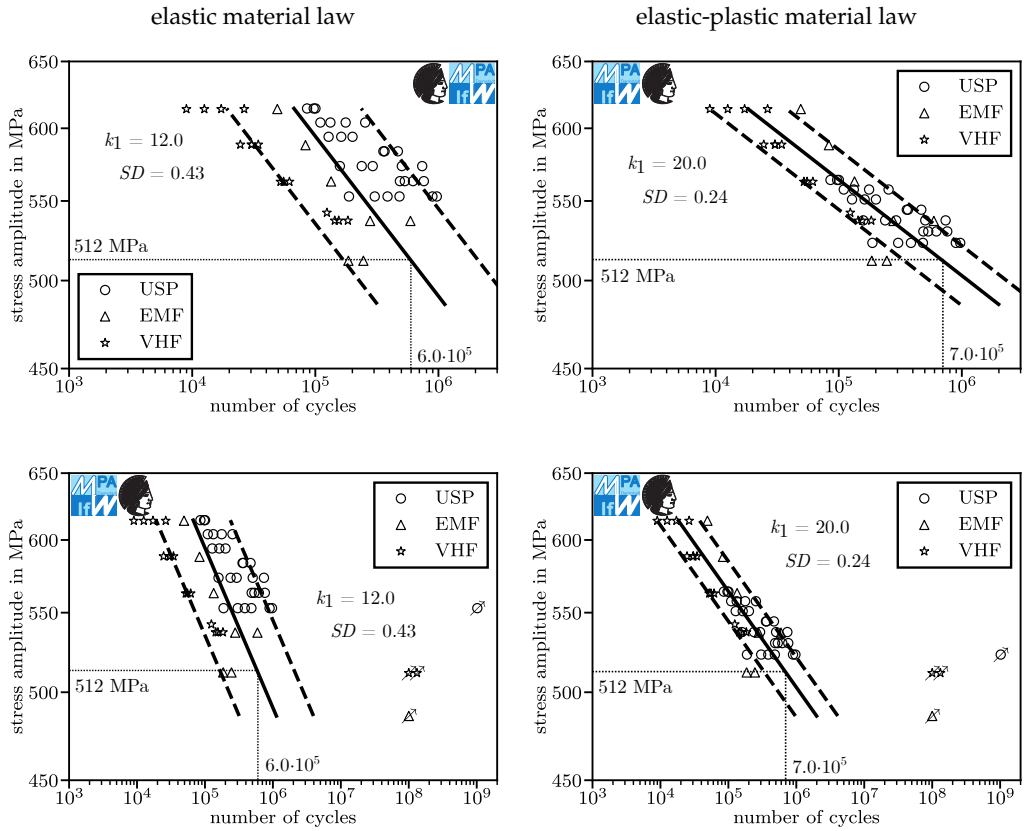

Figure 8. Fatigue behavior of 50CrMo4 in laboratory air; 919 MPa ultimate tensile strength; $K_t = 1$; Curves of 10, 50 and 90% probability of survival; run-outs are marked with an arrow; left side: before correction; right side: after correction; top: only HCF region; bottom: including VHCF region.

In the HCF range (top row of Figure 8), specimens tested with the USP machine last longer at a certain load level compared to the force-controlled machines EMF and VHF, if the stress was calculated using the linear elastic material law (left column). After applying the correction by using the elastic-plastic material law (right column), the USP data points were all moved to a lower load level and agree better with the other results. The EMF and VHF results were not changed. Thereby, the slope exponent increases from $k_1 = 12.0$ to $k_1 = 20.0$ after correction and the standard deviation of the fatigue curve decreases from 0.43 to 0.24. In the bottom row diagram, the VHCF region may be observed. The run-out obtained on the USP is moved closer to the run-outs of the EMF and the VHF. In the corrected data, the results of the VHF occur earlier than results obtained on the other testing setups, except the lowest load level of the EMF.

To objectively evaluate whether the improvement of the fit is significant, a *t*-test is conducted against the null-hypothesis that the average logarithmic deviation of the fracture events from the 50% lifetime prediction is the same for both the evaluation with correction and the evaluation without correction. The logarithmic deviation is measured horizontally. Since both curves are obtained using the same specimens, a paired-sample test is conducted. With predicted logarithmic lifetimes according to the model with correction $N_{\log,\text{predicted,corr},i}$ and according to the model without correction $N_{\log,\text{predicted,no\_corr},i}$ as well as the measured lifetimes $N_{\log,\text{fracture},i}$, differences in logarithmic prediction error $\Delta N_{\log,i}$ are computed and used to compute the *t*-statistic and the *p*-value according to statistical standard theory utilizing the Python module SciPy [124].

$$\Delta N_{\log,i} = |N_{\log,\text{fracture},i} - N_{\log,\text{predicted,corr},i}| - |N_{\log,\text{fracture},i} - N_{\log,\text{predicted,no\_corr},i}| \quad (9)$$

The null hypothesis H_0 and the hypothesis H_1 are mathematically defined as:

$$H_0 : \sum_i \Delta N_{\log,i} = 0 \quad \text{vs.} \quad H_1 : \sum_i \Delta N_{\log,i} \neq 0 \tag{10}$$

Computation yields a t-statistic of 6.3 at 49 degrees of freedom and a p-value 7.5×10^{-6}%. Simplified, a p-value of 7.5×10^{-6}% means: If the true average of $\Delta N_{\log,i}$ was zero, there would be a 7.5×10^{-6}% chance to obtain a mean with a magnitude as great or greater than we actually obtained. Less simplified, this includes the assumption that our estimated standard deviation is true. Overly simplified, we are $100\% - 7.5 \times 10^{-6}\% = 99.99\ldots\%$ certain that the correction for control type leads to models with lower prediction error, which is, strictly speaking, wrong. At a 5% threshold for significance, the difference in prediction quality is statistically significant and the null hypothesis is rejected. Kindly note that this only applies to the batch under investigation, not for 50CrMo4 in general. The average magnitudes of the logarithmic prediction error are 0.376 without and 0.203 with correction.

The observations made about the results presented in Figure 8 also hold true for test results of notched specimens with $K_t = 1.75$ that were quenched and tempered to ultimate tensile strength levels of 919 MPa, tested in laboratory air; see Figure 9. If the stress was calculated using the elastic material law, the USP specimens also last longer at a given stress level. The correction routine decreases the standard deviation from 0.20 to 0.16. The run-outs are moved further apart. Before correction, the fracture events obtained on the VHF occur earlier (tend to be on the left side of the fatigue curve for 50% survival probability) than fracture events obtained on the USP (which tend to be on the right side of the fatigue curve for 50% survival probability). After correction, this relationship is inverted.

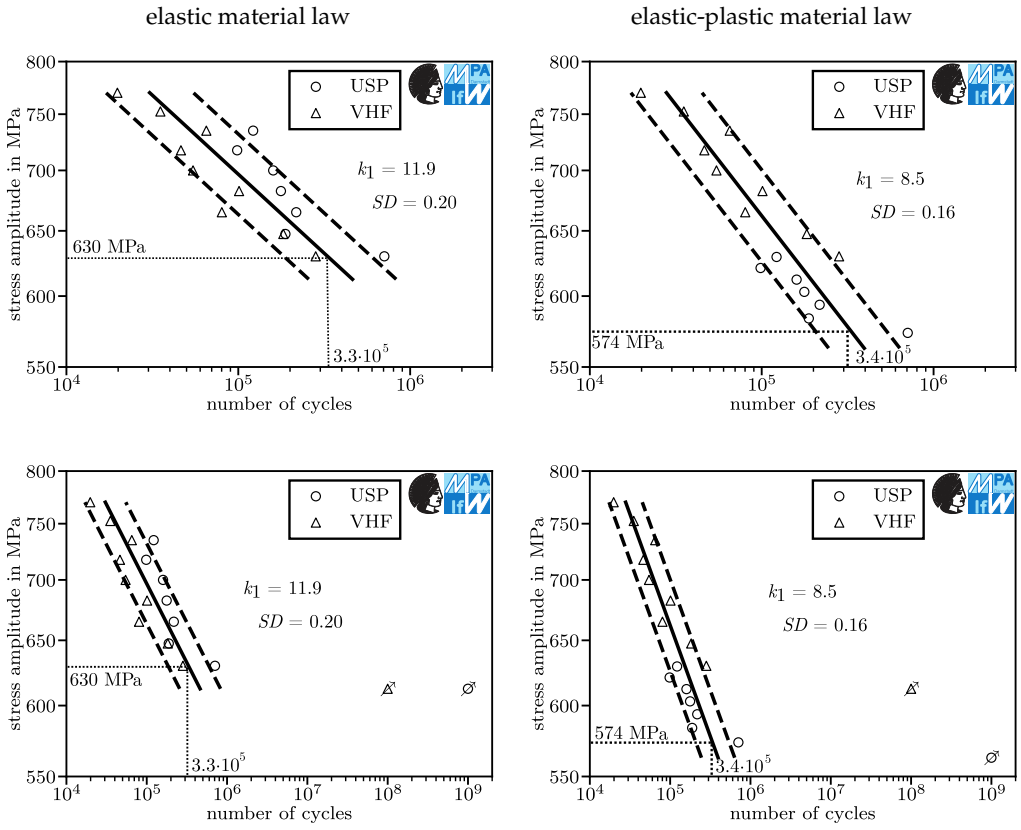

Figure 9. Fatigue behavior of 50CrMo4 in laboratory air; 919 MPa ultimate tensile strength; $K_t = 1.75$; Curves of 10, 50 and 90% probability of survival; run-outs are marked with an arrow; left side: before correction; right side: after correction; top: only HCF region; bottom: including VHCF region.

Testing the difference in logarithmic prediction error $\Delta N_{\log,i}$ according to Equation (9) yields a t-statistic of 1.1 at 15 degrees of freedom and a p-value of 28.8%, which implies that the null hypothesis cannot be rejected based on the data available. Absence of evidence is not evidence of absence. The low p-value may be caused by unfavorable randomness or low number of specimens. Additional tests may yield significant results. The average magnitudes of the logarithmic prediction error are 0.174 without and 0.137 with correction.

Figure 10 shows the results for notched specimens with $K_t = 1.75$ quenched and tempered to ultimate tensile strength levels of 919 MPa, tested in an argon inert gas atmosphere. The diagrams before and after correction show a very similar behavior compared to the previous tests. This data set includes an outlier failure on the VHF. This outlier cannot be explained by the correction method. Kindly note the extremely low standard deviation of 0.11 after correction (ignoring the outlier since it occurred at over 3×10^6 cycles). While we would expect tests in argon to yield results with lower scatter due to a controlled atmosphere, the reduced standard deviation may also be caused by the elimination of extrinsic effects, e.g., oxide-induced crack closure.

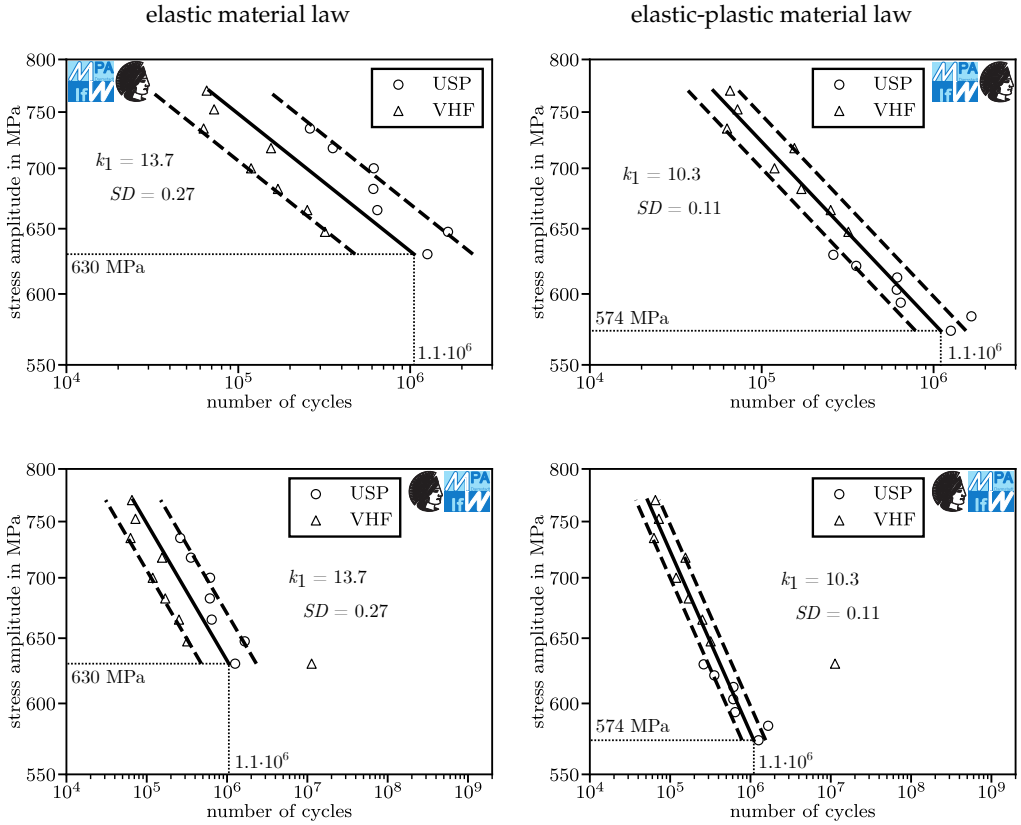

Figure 10. Fatigue behavior of 50CrMo4 in argon; 919 MPa ultimate tensile strength; $K_t = 1.75$; Curves of 10, 50 and 90% probability of survival; run-outs are marked with an arrow; left side: before correction; right side: after correction; top: only HCF region; bottom: including VHCF region.

In fact, if there was a momentous bias between the data obtained on the USP compared to the data obtained on the VHF, the standard deviation would be greater. Therefore, the bias must be small. Consequently, the sum of all intrinsic and extrinsic effects not accounted for is small. The natural conclusion is that the individual effects are small, however more research is necessary to eliminate the possibility that the effects are large and cancel each other out.

Some atmospheric influences, e.g., oxide-induced crack closure, lead to a longer lifetime for low frequencies compared to high frequencies, see Section 2.2. Longer lifetimes at low frequencies can be observed in Figure 9 (laboratory air, 6 out of 7 USP results on the left side of the 50% fatigue curve),

but not in Figure 10 (argon, 4 out of 7 USP results on the left side of the 50% fatigue curve) on the right. The underlying experiments only differ in the atmosphere and the load levels; the specimens were from the same batch. At the current state of research, the atmospheric influences are the best explanation for the difference in lifetime since intrinsic effects can be ruled out, since they would also occur in argon.

The average lifetime of specimens tested in argon is longer than that of specimens tested in lab air all else being equal, Figures 9 and 10. At first, this seems to be in dissent with the observation of different lifetime prolongations due to atmospheric influences. This ostensible contradiction can be explained by the dominance of the effect of the prevention of slip-reversal, which only requires small amounts of oxygen in the atmosphere and does not depend on frequency in lab air because the oxygen concentration there exceeds the necessary concentration by orders of magnitude (for more on this effect, see Section 2.2).

Testing the difference in logarithmic prediction error $\Delta N_{\log,i}$ yields a t-statistic of 2.3 at 15 degrees of freedom and a p-value of 3.5%, which implies significance. The average magnitudes of the logarithmic prediction error are 0.288 without and 0.174 with correction.

Regarding the test results for notched specimens with a stress concentration factor of $K_t = 2.06$, the data obtained in the HCF range show a better agreement, see first row of Figure 11. The fracture events in the VHCF range (second row) also show a higher concordance after correction, but are obviously not comprised within the linear fatigue curve approximation. Hence, a bi-linear approximation of the fatigue curve is necessary to comply with the data, which is out of scope for this paper.

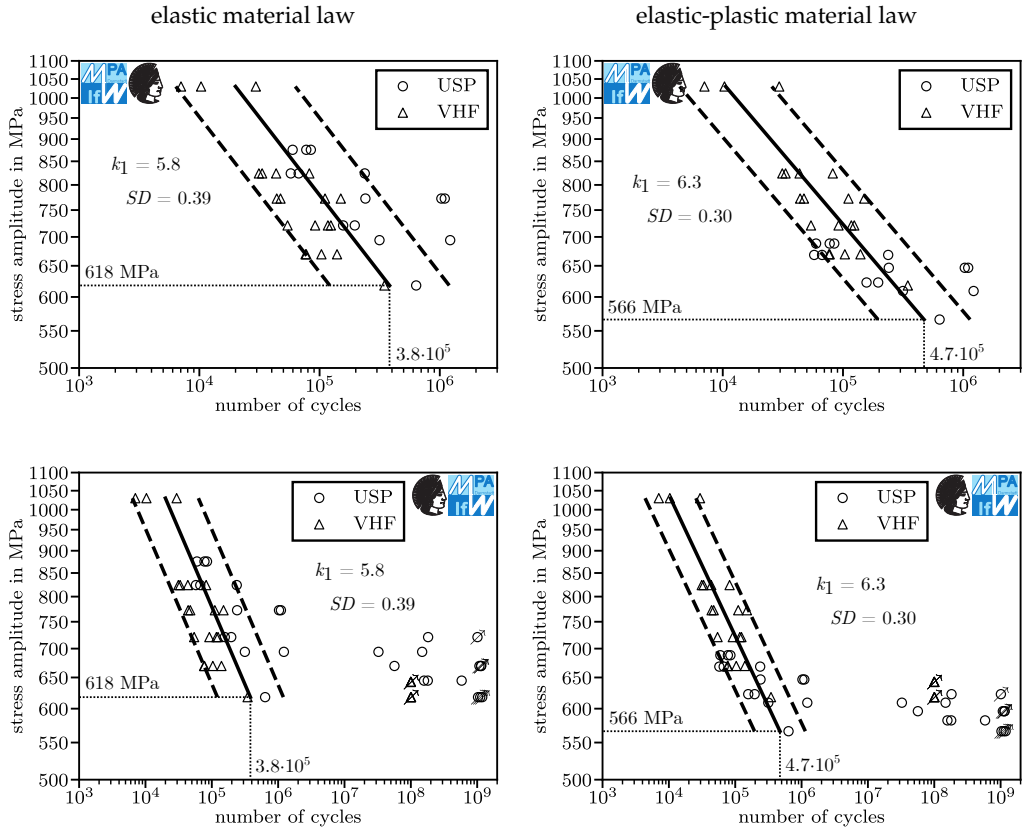

Figure 11. Fatigue behavior of 50CrMo4 in laboratory air; 919 MPa ultimate tensile strength; $K_t = 2.06$; run-outs are marked with an arrow; left side: before correction; right side: after correction; top: only HCF region; bottom: including VHCF region.

Testing the difference in logarithmic prediction error $\Delta N_{\log,i}$ yields a t-statistic of 2.6 at 40 degrees of freedom and a p-value of 1.3%, which implies significance. The average magnitudes of the logarithmic prediction error are 0.719 without and 0.640 with correction.

The results for specimens with a slight stress concentration of $K_t = 1.2$, quenched and tempered to ultimate tensile strength levels of 1096 MPa, tested in laboratory air, are given in Figure 12. In the HCF range, the non-corrected data show a higher lifetime at similar stress levels (around 625 MPa stress amplitude) for tests conducted with the ultrasonic testing machine USPO compared to those obtained with an electromagnetic resonance testing machine (RTTO). After correction, the stress amplitudes match better and the standard deviation reduces—even though there still is a distinct scatter range. Regarding the VHCF range (second row), the stress level of the USPO run-outs is reduced, even though it is still quite high, compared to the results obtained with the RTTO. The observed differences in fatigue behavior are partially or completely caused by differences in specimen geometry. Since the interaction between correction for control type and correction for critically loaded surface area is a nontrivial problem that requires an evaluation of its own, we do not conduct the correction for critically loaded surface area here.

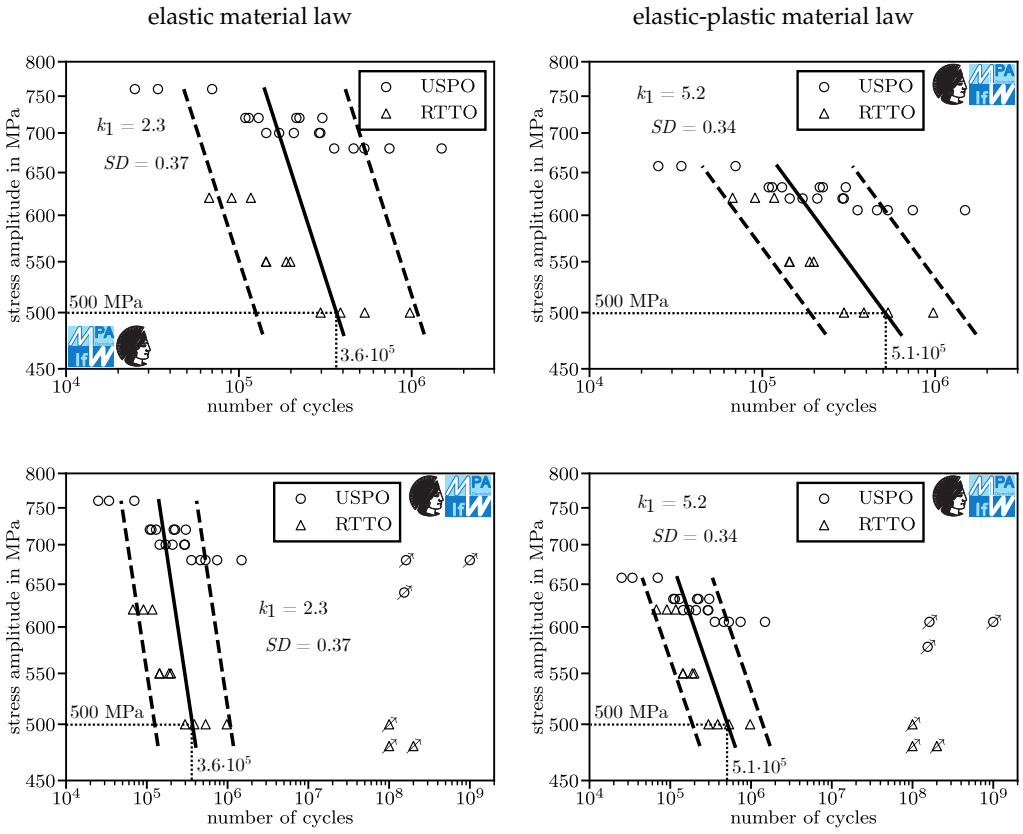

Figure 12. Fatigue behavior of 50CrMo4 in laboratory air; 1096 MPa ultimate tensile strength; $K_t = 1.2$; run-outs are marked with an arrow; left side: before correction; right side: after correction; top: only HCF region; bottom: including VHCF region.

Testing the difference in logarithmic prediction error $\Delta N_{\log,i}$ yields a t-statistic of 1.6 at 29 degrees of freedom and a p-value of 12.2%, which implies rejection of significance. The average magnitudes of the logarithmic prediction error are 0.295 without and 0.276 with correction.

Figure 13 depicts the test results for specimens quenched and tempered to ultimate tensile strength levels of 1726 MPa. Notched specimens with $K_t = 2.06$ were tested in laboratory air. Here, the proposed correction does not show a relevant change because of the comparably high cyclic 0.2% offset yield strength stress and especially high strain rates.

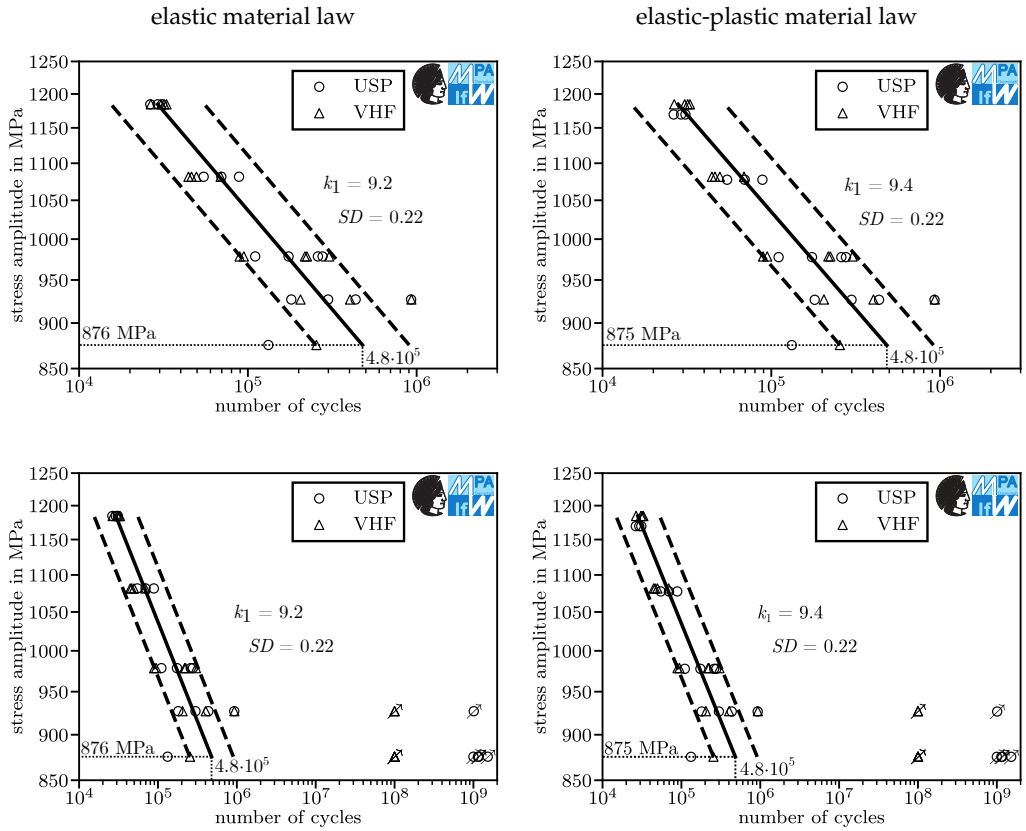

Figure 13. Fatigue behavior of 50CrMo4 in laboratory air; 1726 MPa ultimate tensile strength; $K_t = 2.06$; run-outs are marked with an arrow; left side: before correction; right side: after correction; top: only HCF region; bottom: including VHCF region.

Testing the difference in logarithmic prediction error $\Delta N_{\log,i}$ yields a t-statistic of 1.04 at 31 degrees of freedom and a p-value of 30.5%, which implies rejection of significance. The very high p-value is not surprising because the intersubjective impression is that there is no relevant difference between both data sets. The average magnitudes of the logarithmic prediction error are 0.159 without and 0.162 with correction, meaning that the method for correction worsened prediction quality (insignificantly).

To determine whether there is an overall positive influence on the logarithmic prediction error $\Delta N_{\log,i}$, a t-test according to (10) is conducted using data from all cyclic tests presented above. The test yields a t-statistic of 6.5 at 184 degrees of freedom and a p-value of 7.1×10^{-8}%.

6. Analysis

In Table 4, the parameters of the fatigue curves in Figures 8–13 are summarized. Regarding the slope exponent k_1, there is no trend whether the slope increases or decreases after correction. In all tests conducted, the standard deviation SD decreases or remains unchanged after correction. Furthermore, for all test results, the logarithmic likelihood value $L_{\log}$ increases or remains unchanged, which implies that the corrected regression lines fit the test results better than the non-corrected ones.

Table 4. Parameters, log-likelihood values of fitted fatigue curves as well as number of specimens and *p*-values obtained in *t*-test.

	σ_u	K_t	Atmosphere	Corrected?	σ_{ref}	N_{ref}	k_1	SD	L_{log}	# Specimens *p*-Value
Figure 8	919 MPa	1	lab air	no	512 MPa	6.0×10^5	12.0	0.43	−28.4	50
Figure 8	919 MPa	1	lab air	yes	512 MPa	7.0×10^5	20.0	0.24	−0.4	7.5×10^{-6}%
Figure 9	919 MPa	1.75	lab air	no	630 MPa	3.3×10^5	11.9	0.20	3.2	16
Figure 9	919 MPa	1.75	lab air	yes	574 MPa	3.4×10^5	8.5	0.16	6.5	28.8%
Figure 10	919 MPa	1.75	argon	no	630 MPa	1.1×10^6	13.7	0.27	−1.5	16
Figure 10	919 MPa	1.75	argon	yes	574 MPa	1.1×10^6	10.3	0.11	11.2	3.5%
Figure 11	919 MPa	2.06	lab air	no	618 MPa	3.8×10^5	5.8	0.39	−16.1	41
Figure 11	919 MPa	2.06	lab air	yes	566 MPa	4.7×10^5	6.3	0.30	−7.2	1.3%
Figure 12	1096 MPa	1.2	lab air	no	500 MPa	3.6×10^5	2.3	0.37	−12.34	30
Figure 12	1096 MPa	1.2	lab air	yes	500 MPa	5.1×10^5	5.2	0.34	−10.2	12.2%
Figure 13	1726 MPa	2.06	lab air	no	876 MPa	4.8×10^5	9.2	0.22	3.6	32
Figure 13	1726 MPa	2.06	lab air	yes	875 MPa	4.8×10^5	9.4	0.22	3.6	30.6%

Complementing the intuitive interpretation of Table 4, statistical tests were conducted. A paired-sample *t*-test was conducted for the log-likelihoods. The differences in log-likelihood, 28.0, 3.3, 12.7, 8.9, 2.14 and 0.0, yield a *t*-statistic of 2.17, which translates to a *p*-value of 8.2%. The average difference of the log-likelihoods is 9.2. At a 5% threshold for acceptance of significance, the reduction of log-likelihood is not significant. As per usual in science and especially in statistical testing, absence of evidence is not evidence for absence. In the case of the log-likelihood, this means that the reason for not rejecting the null hypothesis may well be the low sample number of 6 and the high standard deviation which was estimated to be 10.3.

Another paired-sample *t*-test was conducted for the standard deviations. The differences in standard deviation, 0.19, 0.04, 0.16, 0.09, 0.03 and 0.00, yield a *t*-statistic of 2.74, which translates to a *p*-value of 4.1%. Therefore, the reduction of standard deviation is significant considering the threshold of 5%. The average difference in standard deviation is 0.085. This implies that the method for correction for control type significantly decreases standard deviation, not only of the data sets under investigation, but also of all data sets generated in similar tests on batches of 50CrMo4 that are comparable to the ones under investigation.

Testing the average magnitudes of logarithmic prediction error of the six different tests in a paired-sample *t*-test yields a *t*-statistic of 2.68, which translates to a *p*-value of 4.4% at average magnitudes of logarithmic prediction errors of 0.335 without and 0.265 with correction for control type. This also implies significance.

7. Summary

In this study, cyclic test results obtained in displacement-controlled cyclic tests at about 20 kHz were corrected for control type. Two kinds of combined sets were created. The first kind of set contains cyclic test results from force-controlled tests and uncorrected results from displacement-controlled tests. The second kind of set contains cyclic test results from force-controlled tests and control type corrected results from displacement-controlled tests.

The agreement of the cyclic test results with each other inside each data set created this way was quantified through the standard deviation and the likelihood value of a model fitting the data set in the HCF range. Throughout the investigation, the agreements of the data sets with control type corrected data from displacement-controlled tests were equal or superior to the agreements of the data sets with uncorrected data from displacement-controlled tests. This means that the correction method offers significantly improved comparability of displacement-controlled cyclic tests with force-controlled cyclic tests in the HCF range. In the VHCF range, additional investigations are necessary.

8. Outlook

For 50CrMo4, the state of research regarding the influence of the strain rate on the fatigue life may be advanced by incorporating the method presented in this paper. A higher strain rate effect has been reported in low strength 50CrMo4 than in high strength 50CrMo4. However, the difference in strain rate effects may have been overestimated due to an accidental bias in experimental design: the state of research is based on experiments in which low strength 50CrMo4 was tested at load levels momentously exceeding its cyclic yield strength, but high strength 50CrMo4 was tested only at load levels under or just over its cyclic yield strength. In these experiments, strain rate effects cannot be separated from control type effects statistically. An analysis of the experimental data considering and correcting for control type effects would reduce and may practically eliminate the observed difference in strain rate effects. The current state of research is consistent with theoretical considerations: in low strength 50CrMo4, the strain rate dependent Peierls stress makes up a greater share of the total load stress necessary to move a dislocation than in high strength 50CrMo4. Stresses caused by nearby dislocations do not depend on strain rate. However, this does not include any prediction of the size of the strain rate effect, therefore a strain rate effect close to zero in low strength 50CrMo4 would also be consistent with theoretical considerations. Especially the extremely low standard deviation for the specimens tested in argon implies only a small intrinsic strain rate effect for low strength 50CrMo4.

Author Contributions: Conceptualization, M.B.G.; methodology, M.B.G.; software, M.B.G., D.S.L. and J.A.S.; validation, M.B.G. and J.A.S.; formal analysis, M.B.G.; investigation, M.B.G. and M.K.; resources, M.O., M.K. and U.K.; data curation, M.B.G. and A.G.; writing—original draft preparation, M.B.G., M.K. and J.A.S.; writing—review and editing, M.B.G., J.A.S., M.K., D.S.L., A.G., U.K. and M.O.; visualization, M.B.G.; supervision, M.O.; project administration, M.K.; funding acquisition, M.O. All authors have read and agreed to the published version of the manuscript.

Funding: The authors thank the Federal Ministry of Economics and Technology, the German Federation of Industrial Research Associations 'Otto von Guericke' e.V. (BMWi/AiF no. 324ZN and AiF no. 18198 N) and the Forschungskuratorium Maschinenbau e.V. (FKM) for the financial support. We acknowledge support by the German Research Foundation and the Open Access Publishing Fund of Technical University Darmstadt.

Acknowledgments: Some of the data used in this paper was generated by Fraunhofer LBF in BMWi/AiF no. 324ZN and AiF no. 18198. We thank Klaus Störzel and Tobias Melz for the fruitful cooperation.

Conflicts of Interest: The authors declare no conflict of interest.

Appendix A. Do Models Assuming Log-Normal Distributions Describe the Data Sets Well?

In this appendix, we investigate whether models assuming normal distributions describe the data sets under investigation well. To this means, all fatigue events with numbers of cycles to failure 3×10^6 of each test set are shifted to a single virtual load level and compared graphically to the cumulative probability function of the fitted log-normal distribution. The relative numbers of cycles until failure are standardized over the estimated standard deviations, Figures A1–A6.

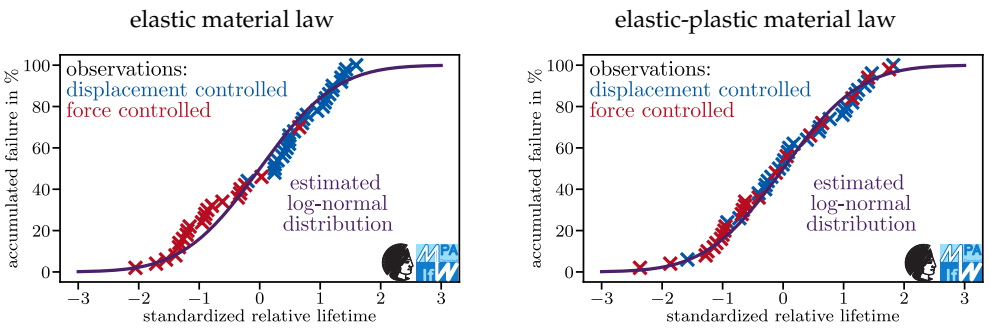

Figure A1. Estimated and observed accumulated failure rates for 50CrMo4 specimens in laboratory air; 919 MPa ultimate tensile strength; $K_t = 1$.

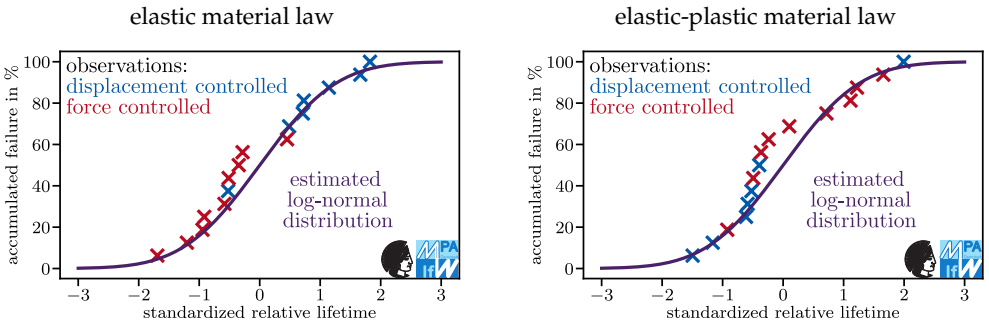

Figure A2. Estimated and observed accumulated failure rates for 50CrMo4 specimens in laboratory air; 919 MPa ultimate tensile strength; $K_t = 1.75$.

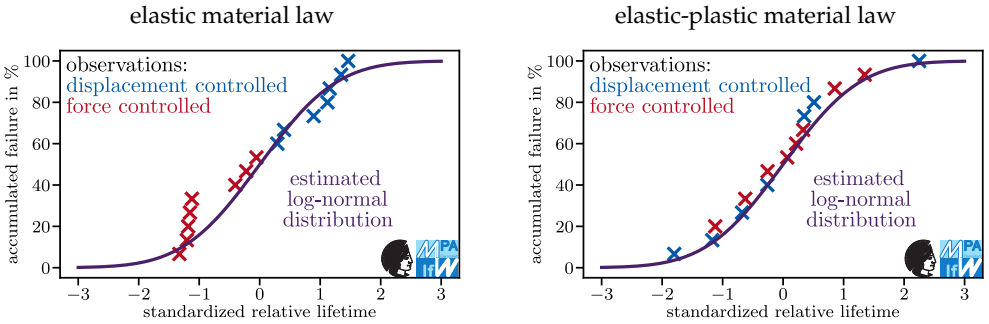

Figure A3. Estimated and observed accumulated failure rates for 50CrMo4 specimens in argon; 919 MPa ultimate tensile strength; $K_t = 1.75$.

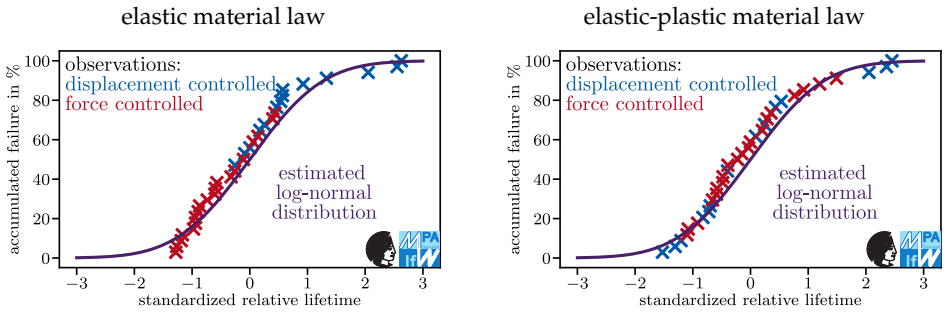

Figure A4. Estimated and observed accumulated failure rates for 50CrMo4 specimens in laboratory air; 919 MPa ultimate tensile strength; $K_t = 2.06$.

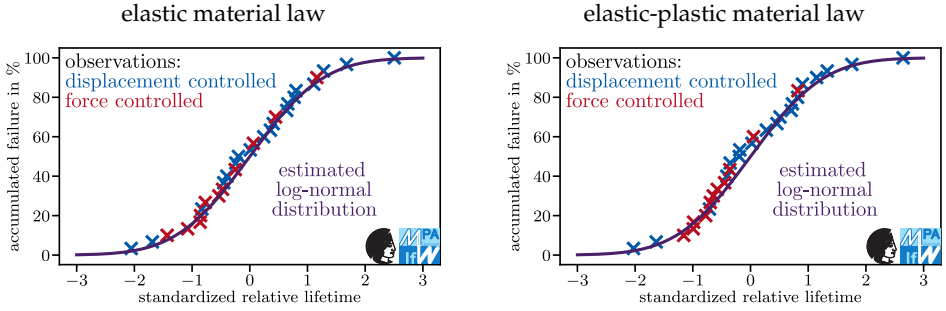

Figure A5. Estimated and observed accumulated failure rates for 50CrMo4 specimens in laboratory air; 1096 MPa ultimate tensile strength; $K_t = 1.2$.

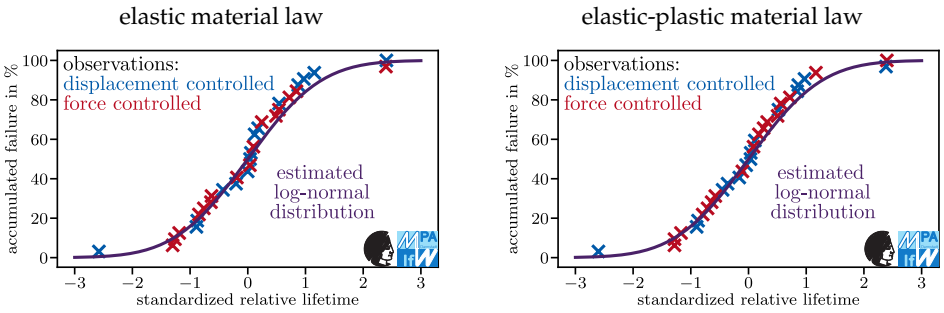

Figure A6. Estimated and observed accumulated failure rates for 50CrMo4 specimens in laboratory air; 1726 MPa ultimate tensile strength; $K_t = 2.06$.

Curves describing the observed accumulated failure rate would run horizontally from each observed data point and jump to the next level just before the next observation. This explains the impression that the estimated log-normal distributions are biased towards higher standardized relative failure rates.

One-sided tendencies of failure events under displacement and force control towards earlier or later lifetimes reflect systematic differences between the results obtained on both experimental setups. Such tendencies are eminent in all non-corrected test results obtained on specimens that were quenched and tempered to ultimate tensile strength levels of 919 MPa.

Quantile-quantile plots are given in Figures A7–A12. These figures show the same as Figures A1–A6, just in a differently scaled coordinate system with switched axes in which the cumulative function of the log-normal distribution is the 45° line. Good compliance with this line means that the data is well described by a normal distribution. In each figure, the p-value of the corresponding Shapiro-Wilk test is given. Low values imply a rejection of the null hypothesis. The null hypothesis is that the data set under investigation follows a log-normal distribution. The power of Shapiro-Wilk tests is lower in data sets with fewer specimens than in data sets with more specimens.

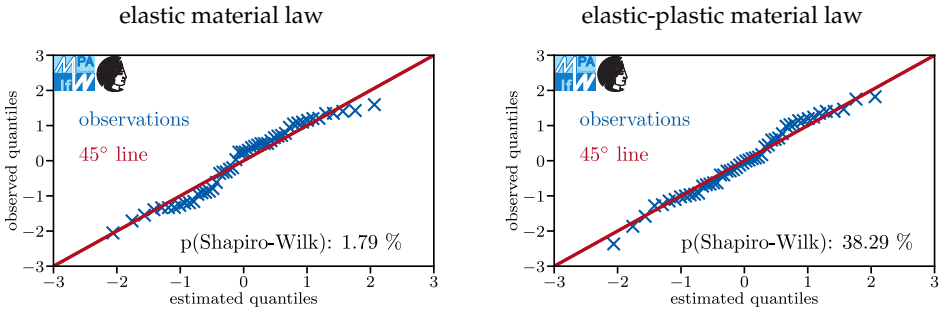

Figure A7. Quantile-quantile plots for 50CrMo4 specimens in laboratory air; 919 MPa ultimate tensile strength; $K_t = 1$.

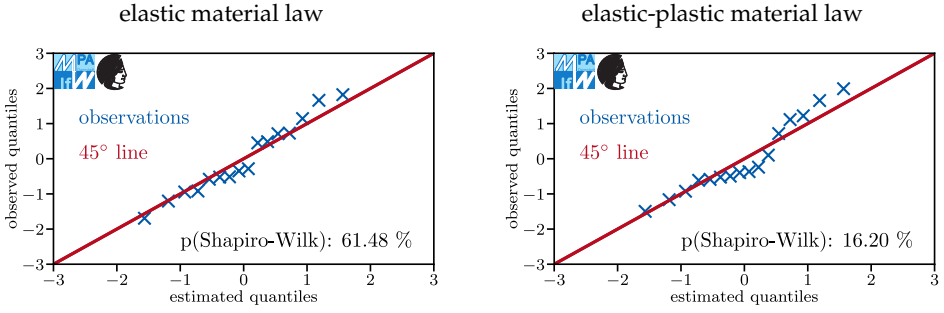

Figure A8. Quantile-quantile plots for 50CrMo4 specimens in laboratory air; 919 MPa ultimate tensile strength; $K_t = 1.75$.

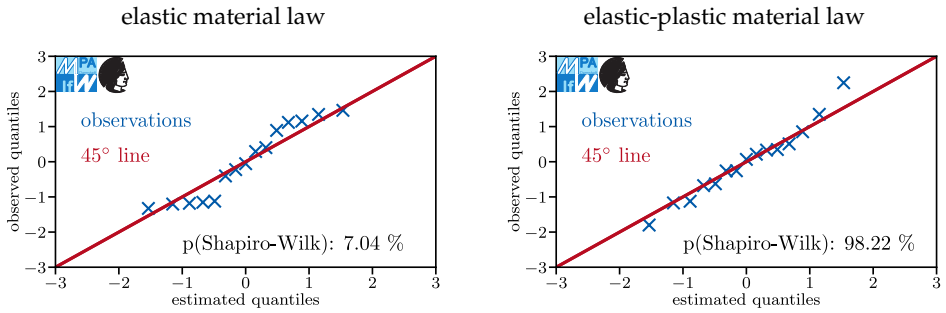

Figure A9. Quantile-quantile plots for 50CrMo4 specimens in argon; 919 MPa ultimate tensile strength; $K_t = 1.75$.

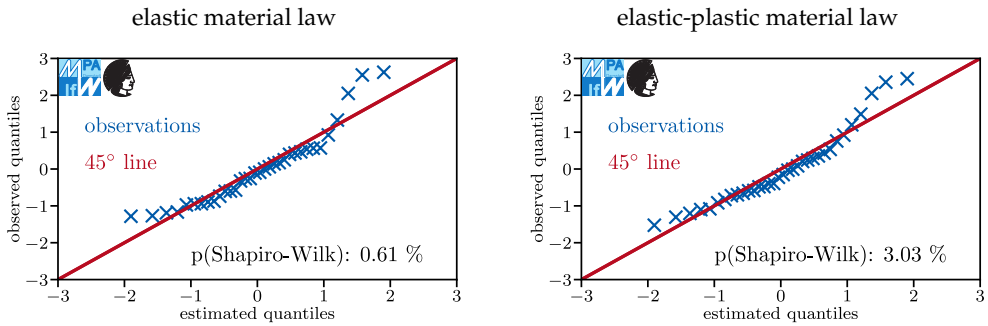

Figure A10. Quantile-quantile plots for 50CrMo4 specimens in laboratory air; 919 MPa ultimate tensile strength; $K_t = 2.06$.

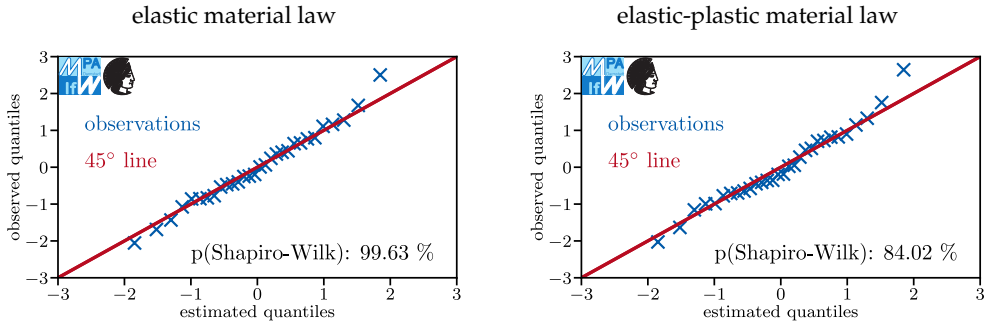

Figure A11. Quantile-quantile plots for 50CrMo4 specimens in laboratory air; 1096 MPa ultimate tensile strength; $K_t = 1.2$.

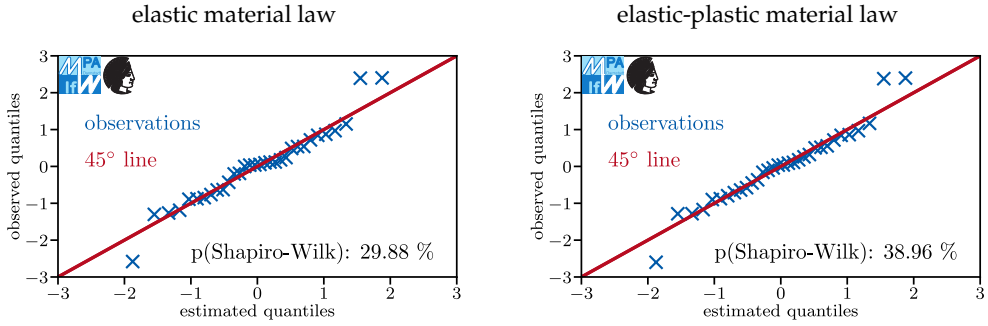

Figure A12. Quantile-quantile plots for 50CrMo4 specimens in laboratory air; 1726 MPa ultimate tensile strength; $K_t = 2.06$.

Although some systematic deviations are present, overall, the data sets agree with the models based on constant log-normal distributions, which implies that the assumption of a log-normal distribution is reasonable. This does not mean that the homoscedastic log-normal distribution is a good model overall. Actually, problems about model consistency and accordance to reality have been brought up in literature [81,125–131]. At a significance level of 5%, the Shapiro-Wilk test rejects normality for three out of twelve data sets.

References

1. Dowling, N.E. *Mechanical Behavior of Materials: Engineering Methods for Deformation, Fracture, and Fatigue*; Pearson: Boston, MA, USA, 2012.
2. Bathias, C. There is no infinite fatigue life in metallic materials. *Fatigue Fract. Eng. Mater. Struct.* **1999**, *22*, 559–565. [CrossRef]
3. Bathias, C.; Drouillac, L.; Le Francois, P. How and why the fatigue S-N curve does not approach a horizontal asymptote. *Int. J. Fatigue* **2001**, *23*, 143–151. [CrossRef]
4. Schwerdt, D. *Schwingfestigkeit und Schädigungsmechanismen der Aluminiumlegierungen EN AW-6056 und EN AW-6082 sowie des Vergütungsstahls 42CrMo4 bei sehr hohen Schwingspielzahlen*; TU Darmstadt: Darmstadt, Germany, 2011.
5. Oechsner, M.; Hanselka, H.; Schneider, N.; Eufinger, J.; Pyttel, B.; Berger, C. *Schlussbericht zu BMWi 324 ZN: Bauteilauslegung unter Berücksichtigung von Beanspruchungen mit variablen Amplituden und sehr hohen Schwingspielzahlen*; MPA-IfW—Technische Universität Darmstadt: Darmstadt, Germany, 2012.
6. Schneider, N. Ermüdungsfestigkeit bei sehr hohen Schwingspielzahlen unter Berücksichtigung des Einflusses der Prüffrequenz. Ph.D. Thesis, TU Darmstadt, Darmstadt, Germany, 2014.
7. Schneider, N.; Schwerdt, D.; Wuttke, U.; Oechsner, M. Fatigue at high number of cyclic loads: Testing methods and failure mechanism. *Mater. Und Werkst.* **2015**, *46*, 931–941. [CrossRef]
8. Krupp, U.; Giertler, A.; Koschella, K. Microscopic Damage Evolution During Very High Cycle Fatigue (VHCF) of Tempered Martensitic Steel. *Procedia Eng.* **2016**, *160*, 231–238. [CrossRef]
9. Schneider, N.; Bödecker, J.; Berger, C.; Oechsner, M. Frequency effect and influence of testing technique on the fatigue behaviour of quenched and tempered steel and aluminium alloy. *Int. J. Fatigue* **2016**, *93*, 224–231. [CrossRef]
10. Oechsner, M.; Melz, T.; Kaffenberger, M.; Störzel, K. *Schlussbericht zu AiF A 18198 N: Bauteilauslegung unter Berücksichtigung von Beanspruchungen mit variablen Amplituden und sehr hohen Schwingspielzahlen*; MPA-IfW—Technische Universität Darmstadt: Darmstadt, Germany, 2017.
11. Pyttel, B.; Brunner, I.; Kaiser, B.; Berger, C.; Mahendran, M. Fatigue behaviour of helical compression springs at a very high number of cycles—Investigation of various influences. *Int. J. Fatigue* **2014**, *60*, 101–109. [CrossRef]
12. Pyttel, B.; Fernández Canteli, A.; Argente Ripoll, A. Comparison of different statistical models for description of fatigue including very high cycle fatigue. *Int. J. Fatigue* **2016**, *93*, 435–442. [CrossRef]
13. Mayer, H.; Schuller, R.; Karr, U.; Fitzka, M.; Irrasch, D.; Hahn, M.; Bacher-Höchst, M. Mean stress sensitivity and crack initiation mechanisms of spring steel for torsional and axial VHCF loading. *Int. J. Fatigue* **2016**, *93*, 309–317. [CrossRef]
14. Mayer, H. Recent developments in ultrasonic fatigue. *Fatigue Fract. Eng. Mater. Struct.* **2016**, *39*, 3–29. [CrossRef]
15. Jeddi, D.; Palin-Luc, T. A review about the effects of structural and operational factors on the gigacycle fatigue of steels. *Fatigue Fract. Eng. Mater. Struct.* **2018**, *41*, 969–990. [CrossRef]
16. Bach, J. Ermüdungsverhalten von Niedrig Legierten Stählen im HCF-und VHCF-Bereich. Ph.D. Thesis, Friedrich-Alexander-Universität Erlangen-Nürnberg, Erlangen, Germany, 2018.
17. Bach, J.; Göken, M.; Höppel, H.W. Fatigue of low alloyed carbon steels in the HCF/VHCF-regimes. In *Fatigue of Materials at Very High Numbers of Loading Cycles*; Springer Fachmedien Wiesbaden: Wiesbaden, Germany, 2018; pp. 1–23.
18. Cai, Y.; Zhao, Y.; Ma, X.; Yang, Z.; Ding, Y. An extended model for fatigue life prediction and acceleration considering load frequency effect. *IEEE Access* **2018**, *6*, 21064–21074. [CrossRef]

19. Hu, Y.; Sun, C.; Xie, J.; Hong, Y. Effects of loading frequency and loading type on high-cycle and very-high-cycle fatigue of a high-strength steel. *Materials* **2018**, *11*, 1456. [CrossRef] [PubMed]
20. Geilen, M.B.; Klein, M.; Oechsner, M. Very high cycle fatigue behaviour of compression springs under constant and variable amplitude loading. *Mater. Und Werkst.* **2019**, *50*, 1301–1316. [CrossRef]
21. Geilen, M.B.; Klein, M.; Oechsner, M.; Kaffenberger, M.; Störzel, K.; Melz, T. A Method for the Strain Rate Dependent Correction for Control Type of Fatigue Tests. *Int. J. Fatigue* **2020**, *138*, 105726. [CrossRef]
22. Atrens, A.; Hoffelner, W.; Duerig, T.W.; Allison, J.E. Subsurface crack initiation in high cycle fatigue in Ti6A14V and in a typical martensitic stainless steel. *Scr. Metall.* **1983**, *17*, 601–606. [CrossRef]
23. Furuya, Y.; Matsuoka, S.; Abe, T.; Yamaguchi, K. Gigacycle fatigue properties for high-strength low-alloy steel at 100 Hz, 600 Hz, and 20 kHz. *Scr. Mater.* **2002**, *46*, 157–162. [CrossRef]
24. Furuya, Y.; Matsuoka, S. Gigacycle fatigue properties of a modified-ausformed Si-Mn steel and effects of microstructure. *Metall. Mater. Trans. A* **2004**, *35*, 1715–1723. [CrossRef]
25. Tsutsumi, N.; Murakami, Y.; Doquet, V. Effect of test frequency on fatigue strength of low carbon steel. *Fatigue Fract. Eng. Mater. Struct.* **2009**, *32*, 473–483. [CrossRef]
26. Müller-Bollenhagen, C.; Zimmermann, M.; Christ, H.J. Adjusting the very high cycle fatigue properties of a metastable austenitic stainless steel by means of the martensite content. *Procedia Eng.* **2010**, *2*, 1663–1672. [CrossRef]
27. Pyttel, B.; Schwerdt, D.; Berger, C. Fatigue strength and failure mechanisms in the VHCF-region for quenched and tempered steel 42CrMoS4 and consequences to fatigue design. *Procedia Eng.* **2010**, *2*, 1327–1336. [CrossRef]
28. Setowaki, S.; Ichikawa, Y.; Nonaka, I. Effect of frequency on high cycle fatigue strength of railway axle steel. In Proceedings of fifth International Conference on Very High Cycle Fatigue, VHCF5, Berlin, Germany, 28–30 June 2011; pp. 153–158.
29. Nonaka, I.; Setowaki, S.; Ichikawa, Y. Effect of load frequency on high cycle fatigue strength of bullet train axle steel. *Int. J. Fatigue* **2014**, *60*, 43–47. [CrossRef]
30. Guennec, B.; Ueno, A.; Sakai, T.; Takanashi, M.; Itabashi, Y. Effect of the loading frequency on fatigue properties of JIS S15C low carbon steel and some discussions based on micro-plasticity behavior. *Int. J. Fatigue* **2014**, *66*, 29–38. [CrossRef]
31. Zhu, M.L.; Liu, L.L.; Xuan, F.Z. Effect of frequency on very high cycle fatigue behavior of a low strength Cr–Ni–Mo–V steel welded joint. *Int. J. Fatigue* **2015**, *77*, 166–173. [CrossRef]
32. Torabian, N.; Favier, V.; Dirrenberger, J.; Adamski, F.; Ziaei-Rad, S.; Ranc, N. Correlation of the high and very high cycle fatigue response of ferrite based steels with strain rate-temperature conditions. *Acta Mater.* **2017**, *134*, 40–52. [CrossRef]
33. Mayer, H.; Papakyriacou, M.; Pippan, R.; Stanzl-Tschegg, S. Influence of loading frequency on the high cycle fatigue properties of AlZnMgCu1. 5 aluminium alloy. *Mater. Sci. Eng. A* **2001**, *314*, 48–54. [CrossRef]
34. Papakyriacou, M.; Mayer, H.; Pypen, C.; Plenk, H., Jr.; Stanzl-Tschegg, S. Influence of loading frequency on high cycle fatigue properties of bcc and hcp metals. *Mater. Sci. Eng. A* **2001**, *308*, 143–152. [CrossRef]
35. Mayer, H.; Ede, C.; Allison, J.E. Influence of cyclic loads below endurance limit or threshold stress intensity on fatigue damage in cast aluminium alloy 319-T7. *Int. J. Fatigue* **2005**, *27*, 129–141. [CrossRef]
36. Engler-Pinto, C.C., Jr.; Frisch Sr, R.J.; Lasecki, J.V.; Mayer, H.; Allison, J.E. Effect of frequency and environment on high cycle fatigue of cast aluminum alloys. In Proceedings of the VHCF-Fourth International Conference on Very High Cycle Fatigue, Ann Arbor, MI, USA, 19–22 August 2007; pp. 421–427.
37. Takeuchi, E.; Furuya, Y.; Nagashima, N.; Matsuoka, S. The effect of frequency on the giga–cycle fatigue properties of a Ti–6Al–4V alloy. *Fatigue Fract. Eng. Mater. Struct.* **2008**, *31*, 599–605. [CrossRef]
38. Zhu, X.; Jones, J.W.; Allison, J.E. Effect of frequency, environment, and temperature on fatigue behavior of E319 cast aluminum alloy: Stress-controlled fatigue life response. *Metall. Mater. Trans. A* **2008**, *39*, 2681–2688. [CrossRef]
39. Begum, S.; Chen, D.L.; Xu, S.; Luo, A.A. Effect of strain ratio and strain rate on low cycle fatigue behavior of AZ31 wrought magnesium alloy. *Mater. Sci. Eng. A* **2009**, *517*, 334–343. [CrossRef]
40. Protz, R.; Kosmann, N.; Gude, M.; Hufenbach, W.; Schulte, K.; Fiedler, B. Voids and their effect on the strain rate dependent material properties and fatigue behaviour of non-crimp fabric composites materials. *Compos. Part B Eng.* **2015**, *83*, 346–351. [CrossRef]

41. Jost, B.; Klein, M.; Beck, T.; Eifler, D. Temperature dependent cyclic deformation and fatigue life of EN-GJS-600 (ASTM 80-55-06) ductile cast iron. *Int. J. Fatigue* **2017**, *96*, 102–113. [CrossRef]
42. Jost, B.; Klein, M.; Beck, T.; Eifler, D. Temperature and frequency influence on the cyclic deformation behavior of EN-GJS-600 (ASTM 80-55-06) ductile cast iron at 0.005 and 5 Hz. *Int. J. Fatigue* **2018**, *110*, 225–237. [CrossRef]
43. Wang, M.; Pang, J.C.; Liu, H.Q.; Zou, C.L.; Li, S.X.; Zhang, Z.F. Deformation mechanism and fatigue life of an Al-12Si alloy at different temperatures and strain rates. *Int. J. Fatigue* **2019**, *127*, 268–274. [CrossRef]
44. Campbell, J.D.; Ferguson, W.G. The temperature and strain-rate dependence of the shear strength of mild steel. *Philos. Mag.* **1970**, *21*, 63–82. [CrossRef]
45. Jaske, C.E.; Leis, B.N.; Pugh, C.E. Monotonic and cyclic stress-strain response of annealed 2 1/4 Cr–1 Mo steel; Oak Ridge National Lab, Tenn. USA, 1975.
46. El-Magd, E. Influence of strain rate on ductility of metallic materials. *Steel Res.* **1997**, *68*, 67–71. [CrossRef]
47. Bleck, W.; Schael, I. Determination of crash–relevant material parameters by dynamic tensile tests. *Steel Res.* **2000**, *71*, 173–178. [CrossRef]
48. Børvik, T.; Hopperstad, O.S.; Berstad, T. On the influence of stress triaxiality and strain rate on the behaviour of a structural steel. Part II. Numerical study. *Eur. J. Mech.-A/Solids* **2003**, *22*, 15–32. [CrossRef]
49. Hopperstad, O.S.; Børvik, T.; Langseth, M.; Labibes, K.; Albertini, C. On the influence of stress triaxiality and strain rate on the behaviour of a structural steel. Part I. Experiments. *Eur. J. Mech.-A/Solids* **2003**, *22*, 1–13. [CrossRef]
50. Lee, W.S.; Liu, C.Y. The effects of temperature and strain rate on the dynamic flow behaviour of different steels. *Mater. Sci. Eng. A* **2006**, *426*, 101–113. [CrossRef]
51. Böhme, W.; Luke, M; Blauel, J. G.; Sun, D.- Z. Rohr, I.; Harwick, W *FAT-Richtlinie Dynamische Werkstoffkennwerte für die Crashsimulation*; FAT-Schriftenreihe: Frankfurt am Main, Germany, 2007; Volume 211.
52. Emde, T. *Mechanisches Verhalten metallischer Werkstoffe über weite Bereiche der Dehnung, der Dehnrate und der Temperatur*; Verlagshaus Mainz GmbH: Aachen, Germany, 2009.
53. Benson, D.K.; Hancock, J.R. The effect of strain rate on the cyclic response of metals. *Metall. Trans.* **1974**, *5*, 1711–1715. [CrossRef]
54. Pineau, A.; Benzerga, A.A.; Pardoen, T. Failure of metals I: Brittle and ductile fracture. *Acta Mater.* **2016**, *107*, 424–483. [CrossRef]
55. Hodowany, J.; Ravichandran, G.; Rosakis, A.J.; Rosakis, P. Partition of plastic work into heat and stored energy in metals. *Exp. Mech.* **2000**, *40*, 113–123. [CrossRef]
56. Cho, K.M.; Lee, S.; Nutt, S.R.; Duffy, J. Adiabatic shear band formation during dynamic torsional deformation of an HY-100 steel. *Acta Metall. Mater.* **1993**, *41*, 923–932. [CrossRef]
57. Kapoor, R.; Nemat-Nasser, S. Determination of temperature rise during high strain rate deformation. *Mech. Mater.* **1998**, *27*, 1–12. [CrossRef]
58. Rosakis, P.; Rosakis, A.J.; Ravichandran, G.; Hodowany, J. A thermodynamic internal variable model for the partition of plastic work into heat and stored energy in metals. *J. Mech. Phys. Solids* **2000**, *48*, 581–607. [CrossRef]
59. Holzer, A.J.; Brown, R.H. Mechanical behavior of metals in dynamic compression. *J. Eng. Mater. Technol.* **1979**, *101*, 238–247. [CrossRef]
60. Klepaczko. An experimental technique for shear testing at high and very high strain rates. The case of a mild steel. *Int. J. Impact Eng.* **1994**, *15*, 25–39. [CrossRef]
61. Johnson, G.R.; Cook, W.H. Fracture characteristics of three metals subjected to various strains, strain rates, temperatures and pressures. *Eng. Fract. Mech.* **1985**, *21*, 31–48. [CrossRef]
62. Zerbst, U.; Vormwald, M.; Pippan, R.; Gänser, H.P.; Sarrazin-Baudoux, C.; Madia, M. About the fatigue crack propagation threshold of metals as a design criterion–a review. *Eng. Fract. Mech.* **2016**, *153*, 190–243. [CrossRef]
63. Tanaka, H.; Homma, N.; Matsuoka, S.; Murakami, Y. Effect of hydrogen and frequency on fatigue behavior of SCM435 steel for storage cylinder of hydrogen station. *Nihon Kikai Gakkai Ronbunshu Hen/Trans. Jpn. Soc. Mech. Eng. Part A* **2007**, *73*, 1358–1365.
64. Murakami, Y.; Matsuoka, S. Effect of hydrogen on fatigue crack growth of metals. *Eng. Fract. Mech.* **2010**, *77*, 1926–1940. [CrossRef]

65. Suresh, S.; Ritchie, R.O. Near-threshold fatigue crack propagation: A perspective on the role of crack closure. In *Fatigue Crack Growth Threshold Concepts*; The Metallurgical Society Inc.: Warrendale, PA, USA, 1983.
66. Blom, A.F.; Holm, D.K. An experimental and numerical study of crack closure. *Eng. Fract. Mech.* **1985**, *22*, 997–1011. [CrossRef]
67. Vasudeven, A.K.; Sadananda, K.; Louat, N. A review of crack closure, fatigue crack threshold and related phenomena. *Mater. Sci. Eng. A* **1994**, *188*, 1–22. [CrossRef]
68. Chermahini, R.G.; Shivakumar, K.N.; Newman, J.C., Jr.; Blom, A.F. Three-dimensional aspects of plasticity-induced fatigue crack closure. *Eng. Fract. Mech.* **1989**, *34*, 393–401. [CrossRef]
69. Pippan, R.; Hohenwarter, A. Fatigue crack closure: A review of the physical phenomena. *Fatigue Fract. Eng. Mater. Struct.* **2017**, *40*, 471–495. [CrossRef]
70. Jiang, Y.; Feng, M.; Ding, F. A reexamination of plasticity-induced crack closure in fatigue crack propagation. *Int. J. Plast.* **2005**, *21*, 1720–1740. [CrossRef]
71. Weibull, W. *A Statistical Theory of Strength of Materials*; Generalstabens litografiska anstalts förlag: Stockholm, Sweden, 1939.
72. Kuhn, P. Effect of geometric size on notch fatigue. In *Colloquium on Fatigue*; Springer: Berlin/Heidelberg, Germany, 1956; pp. 131–140.
73. Böhm, J.; Heckel, K. Die Vorhersage der Dauerschwingfestigkeit unter Berücksichtigung des statistischen Größeneinflusses. *Mater. Und Werkst.* **1982**, *13*, 120–128. [CrossRef]
74. Liu, J.; Zenner, H. Berechnung der Dauerschwingfestigkeit unter Berücksichtigung der spannungsmechanischen und statistischen Stützziffer. *Mater. Und Werkst.* **1991**, *22*, 187–196. [CrossRef]
75. Liu, J.; Zenner, H. Berechnung von Bauteilwöhlerlinien unter Berücksichtigung der statistischen und spannungsmechanischen Stützziffer. *Mater. Und Werkst.* **1995**, *26*, 14–21. [CrossRef]
76. Kloos, K.H.; Kaiser, B.; Friederich, H. Einfluß der Probengröße auf das Verformungs–und Versagensverhalten von Vergütungsstahl 42 CrMo 4 unter Schwingbeanspruchung. *Mater. Und Werkst.* **1995**, *26*, 330–336. [CrossRef]
77. Friederich, H.; Kaiser, B.; Kloos, K.H. Anwendung der Fehlstellentheorie nach Weibull zur Berechnung des statistischen Größeneinflusses bei Dauerschwingbeanspruchung. *Mater. Und Werkst.* **1998**, *29*, 178–184. [CrossRef]
78. Bomas, H.; Linkewitz, T.; Mayr, P. Application of a weakest–link concept to the fatigue limit of the bearing steel SAE 52100 in a bainitic condition. *Fatigue Fract. Eng. Mater. Struct.* **1999**, *22*, 733–741. [CrossRef]
79. Makkonen, M. Statistical size effect in the fatigue limit of steel. *Int. J. Fatigue* **2001**, *23*, 395–402. [CrossRef]
80. Flacelière, L.; Morel, F. Probabilistic approach in high–cycle multiaxial fatigue: Volume and surface effects. *Fatigue Fract. Eng. Mater. Struct.* **2004**, *27*, 1123–1135. [CrossRef]
81. Castillo, E.; Fernandez-Canteli, A. *A Unified Statistical Methodology for Modeling Fatigue Damage*; Springer Science & Business Media: Berlin/Heildelberg, Germay, 2009.
82. Hertel, O.; Vormwald, M. Statistical and geometrical size effects in notched members based on weakest-link and short-crack modelling. *Eng. Fract. Mech.* **2012**, *95*, 72–83. [CrossRef]
83. Ai, Y.; Zhu, S.P.; Liao, D.; Correia, J.A.; de Jesus, A.M.P.; Keshtegar, B. Probabilistic modelling of notch fatigue and size effect of components using highly stressed volume approach. *Int. J. Fatigue* **2019**, *127*, 110–119. [CrossRef]
84. Vaara, J.; Väntänen, M.; Kämäräinen, P.; Kemppainen, J.; Frondelius, T. Bayesian analysis of critical fatigue failure sources. *Int. J. Fatigue* **2020**, *130*, 105282. [CrossRef]
85. Rennert, R.; Kullig, E.; Vormwald, M.; Esderts, A.; Siegele, D. *Rechnerischer Festigkeitsnachweis für Maschinenbauteile aus Stahl, Eisenguss- und Aluminiumwerkstoffen*, 6th ed.; FKM-Richtlinie, VDMA Verlag: Frankfurt am Main, Germany, 2012.
86. Fiedler, M.; Wächter, M.; Varfolomeev, I.; Vormwald, M.; Esderts, A. *Rechnerischer Festigkeitsnachweis unter Expliziter Erfassung Nichtlinearen Werkstoffverhaltens für Maschinenbauteile aus Stahl, Stahlguss und Aluminiumknetlöegierungen*, 1st ed.; FKM-Richtlinie, VDMA Verlag: Frankfurt am Main, Germany, 2019.
87. Kletzin, U.; Reich, R.; Oechsner, M.; Spies, A.; Pyttel, B.; Hanning, G.; Rennert, R.; Kullig, E. *Rechnerischer Festigkeitsnachweis für Federn und Federelemente*, 1st ed.; FKM-Richtlinie, VDMA Verlag: Frankfurt am Main, Germany, 2020.
88. Skelton, R.P.; Haigh. Fatigue crack growth rates and thresholds in steels under oxidising conditions. *Mater. Sci. Eng.* **1978**, *36*, 17–25. [CrossRef]

89. Suresh, S.; Zamiski, G.F.; Ritchie, D.R.O. Oxide-induced crack closure: An explanation for near-threshold corrosion fatigue crack growth behavior. *Metall. Mater. Trans. A* **1981**, *12*, 1435–1443. [CrossRef]
90. Liaw, P.K.; Leax, T.R.; Williams, R.S.; Peck, M.G. Influence of oxide-induced crack closure on near-threshold fatigue crack growth behavior. *Acta Metall.* **1982**, *30*, 2071–2078. [CrossRef]
91. Maierhofer, J.; Simunek, D.; Gänser, H.P.; Pippan, R. Oxide induced crack closure in the near threshold regime: The effect of oxide debris release. *Int. J. Fatigue* **2018**, *117*, 21–26. [CrossRef]
92. Riemelmoser, F.O.; Gumbsch, P.; Pippan, R. Dislocation modelling of fatigue cracks: An overview. *Mater. Trans.* **2001**, *42*, 2–13. [CrossRef]
93. Lee, H.H.; Uhlig, H.H. Corrosion fatigue of type 4140 high strength steel. *Metall. Mater. Trans. B* **1972**, *3*, 2949–2957. [CrossRef]
94. Shives, T.R.; Bennett, J.A. *The Effect of Environment on the Fatigue Strengths of Four Selected Alloys*; National Aeronautics and Space Administration: Washington, DC, USA, 1965.
95. Wadsworth, N.J. The influence of atmospheric corrosion on the fatigue limit of iron-0.5% carbon. *Philos. Mag.* **1961**, *6*, 397–401. [CrossRef]
96. Yoshinaka, F.; Nakamura, T. Effect of vacuum environment on fatigue fracture surfaces of high strength steel. *Mech. Eng. Lett.* **2016**, *2*, 15–00730. [CrossRef]
97. Spriestersbach, D. VHCF-Verhalten des hochfesten Stahls 100Cr6: Rissinitiierungsmechanismen und Schwellenwerte. Ph.D. Thesis, TU Kaiserslaurtern, Kaiserslautern, Germany, 2020.
98. Wei, R.; Talda, P.; Li, C.Y. Fatigue-crack propagation in some ultrahigh-strength steels. In *Fatigue Crack Propagation*; ASTM International: West Conshohocken, PA, USA, 1967.
99. Dahlberg, E.P. Fatigue-crack propagation in high-strength 4340 steel in humid air(Water vapor effects on fatigue crack propagation rates in high strength 4340 steel examined by optical and electron fractography). *ASM Trans. Q.* **1965**, *58*, 46–53.
100. Achter, M. Effect of environment on fatigue cracks. In *Fatigue Crack Propagation*; ASTM International: West Conshohocken, PA, USA, 1967.
101. Henaff, G.; Marchal, K.; Petit, J. On fatigue crack propagation enhancement by a gaseous atmosphere: experimental and theoretical aspects. *Acta Metall. Mater.* **1995**, *43*, 2931–2942. [CrossRef]
102. Spriestersbach, D.; Grad, P.; Brodyanski, A.; Lösch, J.; Kopnarski, M.; Kerscher, E. Very high cycle fatigue crack initiation: Investigation of fatigue mechanisms and threshold values for 100Cr6. In *Fatigue of Materials at Very High Numbers of Loading Cycles*; Springer: Berlin, Germany, 2018; pp. 167–210.
103. Thompson, N.; Wadsworth, N.J.; Louat, N. The origin of fatigue fracture in copper. *Philos. Mag.* **1956**, *1*, 113–126. [CrossRef]
104. Duquette, D.J. *Environmental Effects on General Fatigue Resistance and Crack Nucleation in Metals and Alloys*; Technical Report; Office of Naval Research: Troy, NY, USA, 1978.
105. Hudson, C.M.; Seward, S.K. A literature review and inventory of the effects of environment on the fatigue behavior of metals. *Eng. Fract. Mech.* **1976**, *8*, 315–329. [CrossRef]
106. Krupp, U. Mikrostrukturelle Aspekte der Rissinitiierung und-ausbreitung in metallischen Werkstoffen. Habilitation Thesis, Universität Siegen, Siegen, Germany, 2004.
107. Bradhurst, D.H.; Leach, J.L. The mechanical properties of thin anodic films on aluminum. *J. Electrochem. Soc.* **1966**, *113*, 1245. [CrossRef]
108. Grosskreutz, J.C. The effect of oxide films on dislocation-surface interactions in aluminum. *Surf. Sci.* **1967**, *8*, 173–190. [CrossRef]
109. Nakamura, T.; Oguma, H.; Shinohara, Y. The effect of vacuum-like environment inside sub-surface fatigue crack on the formation of ODA fracture surface in high strength steel. *Procedia Eng.* **2010**, *2*, 2121–2129. [CrossRef]
110. Petit, J.; Sarrazin-Baudoux, C. An overview on the influence of the atmosphere environment on ultra-high-cycle fatigue and ultra-slow fatigue crack propagation. *Int. J. Fatigue* **2006**, *28*, 1471–1478. [CrossRef]
111. Murakami, Y.; Nomoto, T.; Ueda, T.; Murakami, Y. On the mechanism of fatigue failure in the superlong life regime (N> 10000000 cycles). Part 1: Influence of hydrogen trapped by inclusions. *Fatigue Fract. Eng. Mater. Struct.* **2000**, *23*, 893–902. [CrossRef]

112. Murakami, Y.; Nomoto, T.; Ueda, T.; Murakami, Y. On the mechanism of fatigue failure in the superlong life regime (N> 10000000 cycles). Part II: Influence of hydrogen trapped by inclusions. *Fatigue Fract. Eng. Mater. Struct.* **2000**, *23*, 903–910. [CrossRef]
113. Barrera, O.; Tarleton, E.; Tang, H.W.; Cocks, A.C. Modelling the coupling between hydrogen diffusion and the mechanical behaviour of metals. *Comput. Mater. Sci.* **2016**, *122*, 219–228. [CrossRef]
114. Barrera, O.; Bombac, D.; Chen, Y.; Daff, T.D.; Galindo-Nava, E.; Gong, P.; Haley, D.; Horton, R.; Katzarov, I.; Kermode. Understanding and mitigating hydrogen embrittlement of steels: A review of experimental, modelling and design progress from atomistic to continuum. *J. Mater. Sci.* **2018**, *53*, 6251–6290. [CrossRef]
115. Giertler, A. Volume 2020, Band 2, Berichte aus dem Institut für Eisenhüttenkunde. In *Mechanismen der Rissentstehung und -ausbreitung im Vergütungsstahl 50CrMo4 bei sehr hohen Lastspielzahlen*; Shaker Verlag: Düren, Germany, 2020.
116. Glaser, A. Mittelspannungseinfluß auf das Verformungsverhalten von Ck 45 und 42 CrMo 4 bei Spannungs-Und Dehnungskontrollierter Homogen-Einachsiger Schwingbeanspruchung. Ph.D. Thesis, KIT, Karlsruhe, Germany, 1988.
117. Ramberg, W.; Osgood, W.R. *Description of Stress-Strain Curves by Three Parameters*; National Advisory Comitee for Aeronatuics: Washington, DC, USA, 1943.
118. Neuber, H. Über die Berücksichtigung der Spannungskonzenlration bei Festigkeitsproblemen. *Konstr. Berl.* **1968**, *20, 245-251*.
119. Topper, T.; Wetzel, R.M.; Morrow, J. *Neuber's Rule Applied to Fatigue of Notched Specimens*; U.S. Naval Air Engineering Center: Philadelphia, PA, USA, 1967.
120. Wächter, M. *Zur Ermittlung von zyklischen Werkstoffkennwerten und Schädigungsparameterwöhlerlinien*; Technische Universität Clausthal: Clausthal-Zellerfeld, Germany, 2016.
121. Müller, C. *Zur Statistischen Auswertung Experimenteller Wöhlerlinien*; Universitätsbibliothek Clausthal: Clausthal-Zellerfeld, Germany, 2015.
122. Müller, C.; Wächter, M.; Masendorf, R.; Esderts, A. Distribution functions for the linear region of the SN curve. *Mater. Test.* **2017**, *59*, 625–629. [CrossRef]
123. Radaj, D.; Vormwald, M. *Ermüdungsfestigkeit*; Springer: Berlin, Germany, 2007.
124. Virtanen, P.; Gommers, R.; Oliphant, T.E.; Haberland, M.; Reddy, T.; Cournapeau, D.; Burovski, E.; Peterson, P.; Weckesser, W.; Bright, J. SciPy 1.0–Fundamental Algorithms for Scientific Computing in Python. *arXiv* **2019**, arXiv:1907.10121.
125. Geilen, M.B.; Klein, M.; Oechsner, M. On the Influence of Ultimate Number of Cycles on Lifetime Prediction for Compression Springs Manufactured from VDSiCr Class Spring Wire. *Materials* **2020**, *13*, 3222. [CrossRef]
126. Bomas, H.; Burkart, K.; Zoch, H.W. Evaluation of S–N curves with more than one failure mode. *Int. J. Fatigue* **2011**, *33*, 19–22. [CrossRef]
127. Paolino, D.S.; Chiangdussi, G.; Rosetto, M. A unified statistical model for S–N fatigue curves: Probabilistic definition. *Fatigue Fract. Eng. Mater. Struct.* **2013**, *36*, 187–201. [CrossRef]
128. Haydn, W.; Schwabe, F. Ermittlung geschlossener probabilistischer Auslegungskennlinien für einstufige Schwingfestigkeitsbeanspruchungen vom LCF- bis VHCF-Bereich. *Mater. Und Werkst.* **2015**, *46*, 591–602. [CrossRef]
129. Fernández-Canteli, A.; Blasón, S.; Pyttel, B.; Muniz-Calvente, M.; Castillo, E. Considerations about the existence or non-existence of the fatigue limit: Implications on practical design. *Int. J. Fract.* **2020**, *223*, 189–196. [CrossRef]
130. Muniz-Calvente, M.; Fernández-Canteli, A.; Pyttel, B.; Castillo, E. Probabilistic assessment of VHCF data as pertaining to concurrent populations using a Weibull regression model. *Fatigue Fract. Eng. Mater. Struct.* **2017**, *40*, 1772–1782. [CrossRef]
131. Kobelev, V. A proposal for unification of fatigue crack growth. *J. Phys. Conf. Ser.* **2018**, *843*, 012022. [CrossRef]